THE DOPING AND TEMPERATURE DEPENDENCE

OF

OPTICAL PROPERTIES OF $ND_{1-X}TIO_3$

THE DOPING AND TEMPERATURE DEPENDENCE

OF

OPTICAL PROPERTIES OF $ND_{1-X}TIO_3$

By

JING YANG, B. Sc.

A Thesis

Submitted to the School of Graduate Studies

in Partial Fulfilment of the Requirements

for the Degree

Master of Science

McMaster University

MASTER OF SCIENCE (2005)   McMaster University

(Physics and Astronomy)   Hamilton, Ontario

TITLE: The Doping and Temperature Dependence

                        of Optical Properties of $Nd_{1-x}TiO_3$

AUTHOR: Jing Yang, B. Sc.

                        Peking University

                        Beijing, P. R. China, 2003

SUPERVISOR: Professor T. Timusk

NUMBER OF PAGES: xi, 68

Abstract

A well characterized titanate system, $Nd_{1-x}TiO_3$, has been studied by temperature dependent reflectance spectroscopy between 50 and 40 000 cm^{-1} at three different doping levels, $x = 0.019, 0.046$, and 0.095, which yield a Mott-Hubbard insulator, a semiconductor and a correlated metal, respectively. Two main issues are discussed regarding the optical properties of the current system. The first is the variation of the low-lying electronic structure with hole concentration. The doping-dependent optical conductivity of $Nd_{1-x}TiO_3$ shows several obvious differences when compared to the superconducting cuprates. We observed mid-infrared absorption bands in the doped samples, suggesting that mid-gap states develop inside the Hubbard gap with hole doping in the context of a two-component model. A quantitative analysis of the spectral weight below 1.2 eV as a function of doping indicates that the evolution rate of the optical excitations below 1.2 eV is related to the electron correlation strength of the parent insulator, which has been observed in other titanates as well. The second issue addressed in this thesis is the temperature-dependent optical features of the correlated metallic sample with $x = 0.095$, a composition close to the metal-insulator transition at $x \sim 0.08$. The optical conductivity shows an anomalous enhancement of spectral weight below 1eV, in both the Drude and midinfrared part, that develops with decreasing temperature. The dynamical mean field theory (DMFT) may explain this feature. Meanwhile, the metallic sample displays a Fermi-liquid like behavior in the low-frequency limit, which can be established from the spectra of the scattering rate as a function of both frequency and temperature. We found a good agreement between the experimental results extracted from the scattering rate and the Fermi-liquid theory.

Acknowledgements

Last but not least, I would like to thank my parents for their love, encouragement, concern and support to me all along.

Contents

List of Figures

List of Tables

Chapter 1

INTRODUCTION

1.1 Transition Metal Oxides — Two Types of Insulators

The transition metal oxides (TMO's) have been extensively studied since many novel and intriguing physical phenomena have been revealed in this series of materials, such as high-T_c superconductivity in the cuprates (Bednorz and Müller, 1986), colossal magnetoresistance (CMR) in the manganites (Schiffer et al., 1994), and the fascinating possibility of combined spin-orbital ordering phenomena (Klejnberg and Spalek, 2000). According to band theory, which is based on noninteracting or weakly interacting electron systems, electrons in a partially filled d-electron band in TMO's are predicted to be de-localization and exhibit metallic properties. However, many TMO's were found to be poor conductors or mostly insulators. Considering a strong Coulomb repulsion between electrons and assuming a lattice model with a single electronic orbital on each site, the Mott-Hubbard theory (Mott, 1949, 1956, 1961, 1974) explains the origin of the insulation behavior of TMO's well. In the theory, two elec-

trons sitting on the same site would feel a large Coulomb repulsion, which would split a single band into two, the lower Hubbard band (LHB), which is formed from electrons that occupied an empty site, and the upper Hubbarb band (UHB), from electrons that occupied a site that is already taken by another electron. With one electron per site, the LHB would be full and the system is an insulator. The energy gap between those two bands was named the correlation energy U. Furthermore, in the TMO's, the excitation energy between the p-band on the anion, O^{2-}, and the empty UHB on the transition-metal cation was called the charge transfer energy Δ. Depending on the relative size of U and Δ, the gap in the TMO's can be of either d-d or d-p character in the scheme of Zaanen-Sawatsky-Allen (ZSA) (Zaanen et al., 1985). For $U > \Delta$, as expected for the heavier transition metals, the lowest charge gap is of d-p type and the compound is a charge-transfer (CT) insulator, while for $U < \Delta$, as for the lighter transition metals, the gap is of a d-d type and the material is a Mott insulator.

1.2   Thesis Motivation and Scope

In transition metal oxides, metal-insulator transitions (MIT), induced by compositional variation, are universal features (Imada et al., 1998). In the Hubbard Model (Hubbard, 1963, 1964a,b), there are two important parameters which correspond to the MIT, the electron correlation strength U/W (W is the one-electron bandwidth.) and the band filling n (the number of d electron per transition-metal cation site). The perovskite-type $Nd_{1-x}TiO_3$ system is one of the best systems for experimentally studying the effect of the $3d$ band filling on the electronic properties during the MIT. Starting from the parent compound $NdTiO_3$, one can introduce vacancies with a concentration of x on the Nd^{3+} site. With a variation of x from 0 to 1/3, the degree of

filling of the $3d$ band of Ti ion can be controlled from 1 ($NdTiO_3$) to 0 ($Nd_{2/3}TiO_3$), since by removing Nd^{3+} by x, Ti^{4+} will increase by $3x$ and equivalently we can consider the band filling n per Ti site is $1 - 3x$ and the hole concentration per Ti site is $3x$. The parent compound, $NdTiO_3$ ($3d^1$), is a Mott insulator (Arima et al., 1993), where the charge gap is determined by the energy difference between the Coulomb-split Hubbard bands. While the other end compound, $Nd_{2/3}TiO_3$, has no d electrons and is a CT insulator with a d-p characterized gap determined by the filled O $2p$ band and the empty Ti $3d$ upper Hubbard band. Two metal-insulator-transitions are expected at doping levels, $x \sim 0.08$ and 0.20 (Sefat, 2005).

Infrared spectroscopy is a powerful tool to probe the spectra of intermediate energy excitations of materials. In this thesis, we use the IR reflectance technique to investigate the variation of the low-lying electronic structures of the titanium oxide system, $Nd_{1-x}TiO_3$, at three doping levels ($x = 0.019, 0.046$, and 0.095), across one of the two MIT points, at various temperatures. In literatures, IR spectra of similar titanium oxide systems, such as $La_{1-x}TiO_3$ (Crandles et al., 1994), $Nd_{1-x}Ca_xTiO_3$ (Katsufuji et al., 1995) etc., have been studied and the $Nd_{1-x}TiO_3$ system exhibits differences and similarities to the above systems. Although a lot of doping-dependent spectra of titanium oxide systems have been intensively investigated, few temperature-dependent spectra study has been done. In this thesis, we presents both the doping and temperature dependence of the optical properties of $Nd_{1-x}TiO_3$.

.

1.3 Samples — Preparation, Properties and Structure

1.3.1 Sample Preparation and Characterization

The micro-twinned single crystals in this study were prepared by Sefat (2005) with two different procedures. The parent compound was grown using the floating-zone method. The doped samples of composition $x \sim 0.046$ and 0.095 were made by a modified Bridgeman process. First, we synthesized polycrystalline samples with the proper stoichiometry by solid state reactions. As the starting material, the polycrystalline powder were then placed in a sealed Molybdenum crucible inside a temperature gradient 'induction furnace'. The temperature was raised to 1800 °C to melt the powder. A drop rod was used as a reference to indicate when the material at the bottom has melted. The furnace was kept at the melting point for some time and then gradually cooled. The melt was crystallized at cool end of the sealed crucible. Neutron activation analysis (NAA) was used to characterize the Nd concentration of the grown samples. A very slight deviation of x from zero in the parent compound was found by NAA and $x = 0.019(6)$. Another two doped samples were considered to be $x = 0.046(10)$ and $x = 0.095(8)$, respectively.

1.3.2 Transport and Magnetic Properties

Four-probe resistivity measurements (Sefat, 2005) indicated that the $x = 0.019$ sample is an insulator and the $x = 0.046$ one shows semiconductor behavior. Because the $x = 0.095$ sample is too small to make contacts on it, the dc resistivity of another piece from the same layer is used to reveal the transport behavior of the piece we did optical measurements on and it points to a metallic transport. The dc resistivity data

of the three samples are displayed in Figure 1.1. According to magnetic susceptibility measurements, both the insulating and semiconducting samples have antiferromagnetism to paramagnetism transitions, around 100 K and 68 K, respectively. However, there is no magnetic transition in the metallic sample (x=0.095).
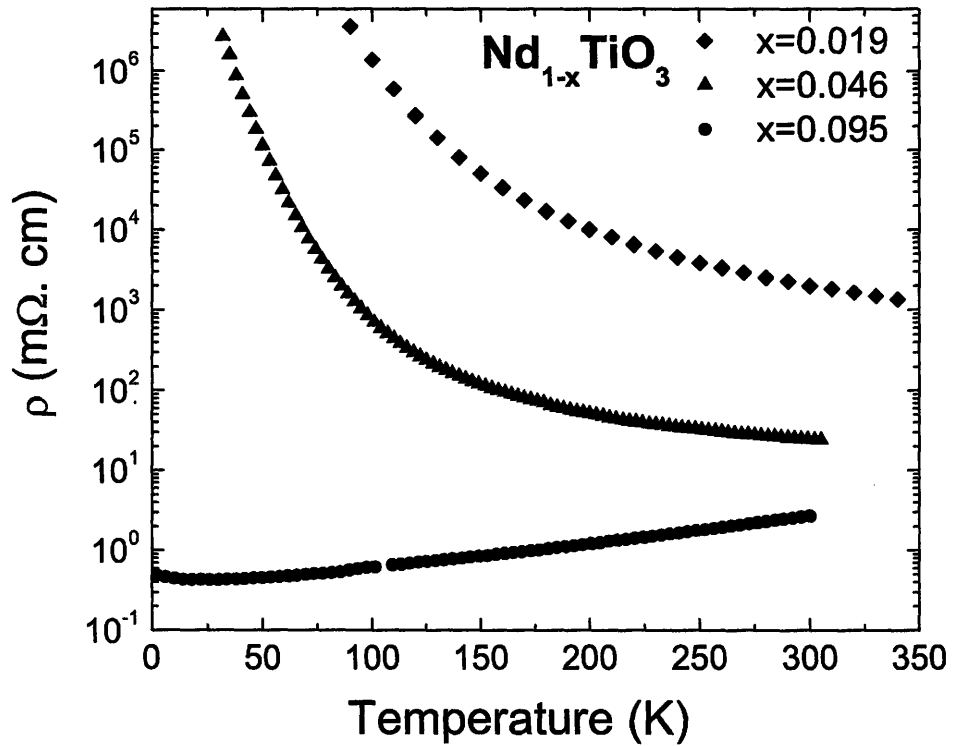
Figure 1.1 DC resistivity data of $x = 0.019, 0.046$ and 0.095 of $Nd_{1-x}TiO_3$ obtained from four-probe resistivity measurements by Sefat (2005).

1.3.3 The Crystal Structure of $Nd_{1-x}TiO_3$

The structure of $Nd_{1-x}TiO_3$ is of a $GdFeO_3$ type with the space group *Pnma*, perovskite with an orthorhombic distortion, as shown in Figure 1.2 (Sefat, 2005). Several titanates have this type of structure (McLean et al., 1979).
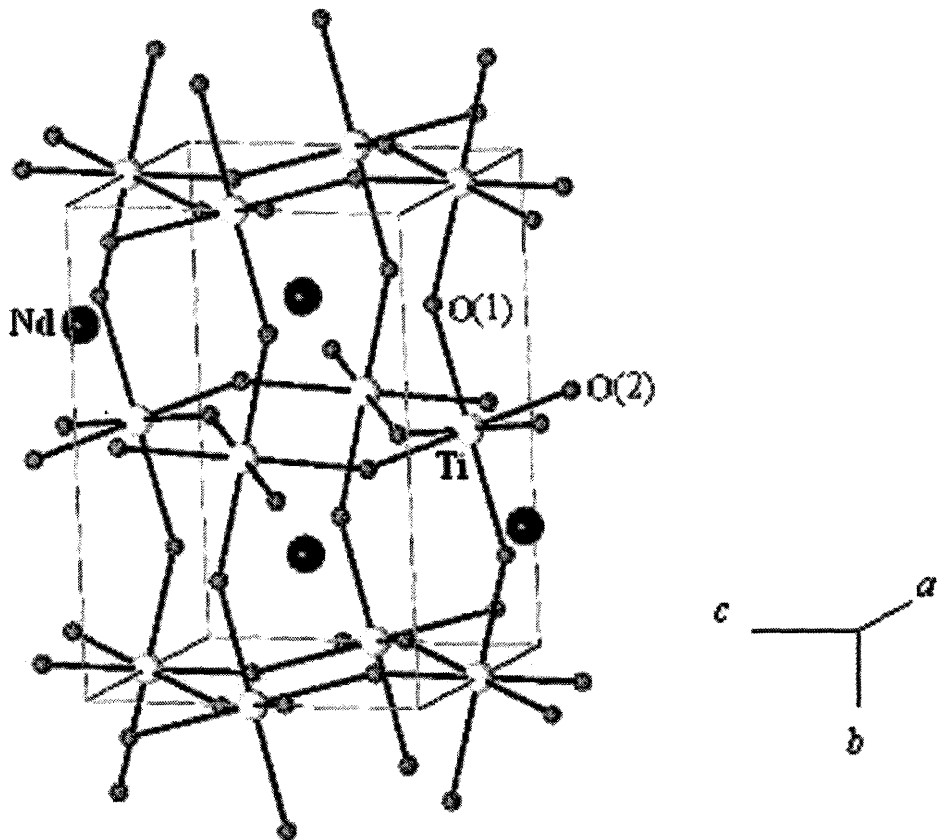
Figure 1.2 Perspective of the *pnma* structure of $Nd_{1-x}TiO_3$.

1.4   Organization of Thesis

This thesis includes five chapters, besides the chapter of Introduction. Chapter 2 presents a brief review of the theoretical background of the IR spectroscopy. Chapter 3 shows the spectrometer and the configuration we used, experimental techniques and improvements to previous instruments. The presentation and discussion of the experimental results of the $Nd_{1-x}TiO_3$ system are displayed in Chapter 4. Chapter 5 includes the conclusions derived from the current work and suggestions for future work. At the end of the thesis, the appendix contains the Matlab programmes for calculating the optical constants appearing in this thesis and the derivation of the Hagen-Rubens relations.

Chapter 2

THEORY AND ANALYTICAL METHODS

2.1   Introduction

This chapter briefly explains the optical response in solids and the theoretical background of two analytical methods used in this thesis. Since the readers can find detailed discussions about the above topics from many books and articles (Kittel, 1976, Timusk and Tanner, 1989), we only introduce essential theory and formulas here.

2.2   Infrared Properties of Solids

2.2.1   Optical Parameters

Experimentally, the reflectance spectra of the samples are the data we directly measured. To uncover the microscopic properties of materials, the electromagnetic

theory of light in solids is used to relate the measured reflectance to the optical constants that can in turn be related to microscopic theories.

For non-magnetic media ($\mu = 1$), the Maxwell's equations can be shown to result in a wave equation for $\mathbf{E}$:

$$\nabla^2 \mathbf{E} = \frac{\epsilon_1}{c^2} \frac{\partial^2 \mathbf{E}}{\partial t^2} + \frac{4\pi\sigma_1}{c^2} \frac{\partial \mathbf{E}}{\partial t}, \tag{2.1}$$

where ϵ_1 the dielectric function, σ_1 the conductivity and c the light velocity. By substituting a plane wave solution

$$\mathbf{E} = \mathbf{E}_0 e^{i(\mathbf{k} \cdot \mathbf{r} - \omega t)} \tag{2.2}$$

into Equation 2.1, one obtains

$$k = \frac{\omega}{c} \sqrt{\epsilon_1 + i \frac{4\pi\sigma_1}{\omega}}. \tag{2.3}$$

The complex refractive index $\tilde{N}$ is then defined as

$$\tilde{N} = \sqrt{\epsilon_1 + i \frac{4\pi\sigma_1}{\omega}} = \sqrt{\epsilon} = \sqrt{\epsilon_1 + i\epsilon_2} = n + i\kappa, \tag{2.4}$$

where, ϵ_1, ϵ_2 are the real and imaginary parts of the complex dielectric function ϵ, n the index of refractive, κ the extinction coefficient. Alternatively, the complex refractive index $\tilde{N}$ has another form in terms of the real and imaginary parts of optical conductivity σ,

$$\tilde{N}^2 = \epsilon_\infty + \frac{4\pi i}{\omega}(\sigma_1 + i\sigma_2), \tag{2.5}$$

where $\epsilon_\infty = 1$. Consequently,

$$\epsilon_1 = n^2 - \kappa^2, \tag{2.6}$$

9

$$\epsilon_2 = 2n\kappa, \tag{2.7}$$

and

$$\sigma_1 = \frac{\omega}{4\pi}\epsilon_2, \tag{2.8}$$

$$\sigma_2 = \frac{\omega}{4\pi}(\epsilon_\infty - \epsilon_1). \tag{2.9}$$

Under the condition of normal incidence in vacuum, the electromagnetic boundary conditions give,

$$r = \frac{\mathbf{E}_r}{\mathbf{E}_i} = \frac{\tilde{N} - 1}{\tilde{N} + 1} = \frac{n + i\kappa - 1}{n + i\kappa + 1}, \tag{2.10}$$

where r is the complex reflection coefficient, $\mathbf{E}_i$ the incident electric field and $\mathbf{E}_r$ the reflected electric field. If we write r in the following form:

$$r = \sqrt{R}e^{i\theta}, \tag{2.11}$$

with R the reflectance and θ the phase factor, one obtains the relation between the optical constants n, κ and the real and imaginary parts of the reflection coefficient from Equations. 2.10-2.11:

$$n(\omega) = \frac{1 - R}{1 + R - 2\sqrt{R}\cos\theta}, \quad \kappa(\omega) = \frac{-2\sqrt{R}\sin\theta}{1 + R - 2\sqrt{R}\cos\theta}. \tag{2.12}$$

Furthermore, the dielectric function ϵ_1, ϵ_2 and optical conductivity σ_1, σ_2 can be easily derived in terms of R and θ from Equations. 2.6-2.9 and 2.12. The calculations of the above optical parameters by Matlab programs are attached as Appendix A for readers' reference. In reality, due to the limited frequency region we can measure, ϵ_∞ is usually found to be a number greater than 1, including the contribution from high-energy interband processes.

The f-sum rule or oscillator-strength sum rule is important to optical spec-

troscopy and it states:

$$\int_0^\infty \sigma_1(\omega')d\omega' = \frac{\pi N e^2}{2m_e} = \frac{\omega_p^2}{8} \qquad (2.13)$$

where N is the total electron density in the material, m_e is the free electron mass, and $\omega_p^2 = \frac{4\pi N e^2}{m_e}$ the optical plasma frequency. The f-sum rule results that the spectral weight, or the area under the curve of σ_1 as a function of ω, of the whole spectrum up to infinity is a constant in terms of factors, such as temperature. Our measurements in Chapter 4 show that there is a transfer of spectral weight from high frequencies to regions of lower frequencies, but the total spectral weight does not change much with temperature. Furthermore, a partial sum rule can be used to determine the number of effective electrons per atom associated with certain excitations when various kinds of electronic excitations are well separated in the conductivity spectra. The partial sum rule is defined as follows,

$$N_{eff}(\omega) = \frac{2m_e V_{atom}}{\pi e^2} \int_0^\omega \sigma_1(\omega')d\omega', \qquad (2.14)$$

with V_{atom} the volume of per atom, N_{eff} the effective electron number per atom in the solid associated with the optical transitions at frequencies below ω. We can estimate the plasma frequency of the conduction electrons in a metal by applying the partial sum rule to the low-frequency conductivity spectra.

2.2.2 Kramers-Kronig Transformations

As discussed in Section 2.2.1, as long as both R and θ are known, one can easily calculate other optical parameters. However, in fact, only the real part of the complex reflection coefficient, R, can be experimentally measured in this work. To

obtain the phase factor, θ, one need to perform the Kramers-Kronig (KK) analysis:

$$\theta(\omega) = \frac{\omega}{\pi} \int_0^\infty \frac{\ln R(\omega') - \ln R(\omega)}{\omega^2 - \omega'^2} d\omega'. \tag{2.15}$$

Note that in order to carry out the KK transformation, the reflectance spectrum covering the whole frequency range is needed.

2.3   Methods of Analyzing the Infrared Conductivity

There are two analytical approaches used to describe the optical-activated excitations in solids, the two-component model and one-component model. Although the two methods treat the infrared conductivity in different ways, so far they are both candidates for interpreting the possible optical processes in the infrared region.

2.3.1   Two-component Model : Drude-Lorentz Oscillators

One of the analytical method is the Drude-Lorentz oscillator, namely the two-component model, which can be deduced from the classical Newton's equation,

$$m\ddot{\mathbf{r}} + m\Gamma\dot{\mathbf{r}} + m\omega_0^2\mathbf{r} = e\mathbf{E}, \tag{2.16}$$

where m is the mass of the electron, Γ the viscous damping term, ω_0 the resonant frequency. Try the solution with $\mathbf{r} = \mathbf{r}_0 e^{-i\omega t}$,

$$\mathbf{r} = \frac{e\mathbf{E}}{m} \frac{1}{\omega_0^2 - \omega^2 - i\omega\Gamma}. \tag{2.17}$$

12

On the other hand, the dielectric function $\epsilon(\omega)$ is defined as,

$$\epsilon(\omega) = \frac{\mathbf{D}}{\mathbf{E}} = \frac{\mathbf{E} + 4\pi\mathbf{P}}{\mathbf{E}}, \tag{2.18}$$

and $\mathbf{P} = eN\mathbf{r}$, where $\mathbf{E}$ is the applied field, $\mathbf{D}$ the total field, $\mathbf{P}$ the induced dipole moment per unit volume and N the density of charge carriers.

As a result of Equations. 2.17 and 2.18, $\epsilon(\omega)$ becomes,

$$\epsilon = 1 + \frac{\omega_p^2}{\omega_0^2 - \omega^2 - i\omega\Gamma} = \epsilon_1 + i\epsilon_2. \tag{2.19}$$

In the Drude model, the case of free electrons without restoring force, the resonant frequency $\omega_0 = 0$ and thus one gets the real and imaginary part of Drude conductivity from Equations 2.8, 2.9 ($\epsilon_\infty = 1$, here) and 2.19 as followings,

$$\sigma_1(\omega) = \frac{\omega_D^2 \Gamma}{4\pi(\omega^2 + \Gamma^2)}, \quad \sigma_2(\omega) = \frac{\omega_D^2 \omega}{4\pi(\omega^2 + \Gamma^2)}. \tag{2.20}$$

Figure 2.1 displays the curves of $\sigma_1(\omega)/\sigma_{DC}$ and $\sigma_2(\omega)/\sigma_{DC}$ from Equation 2.20, where σ_{DC} is a constant, $\sigma_{DC} = \omega_D^2/4\pi\Gamma$.

Equation 2.19 represents the dielectric function of one Lorentz oscillator, and it can be generalized to a series of m oscillators as followings,

$$\epsilon = 1 + \sum_{k=0}^{m-1} \frac{\omega_{pk}^2}{\omega_k^2 - \omega^2 - i\omega\Gamma_k}. \tag{2.21}$$

As displayed in Equation 2.21, in the two-component model, the optical conductivity is considered to be a combination of free and bound carriers. The free-carrier component is fit to the Drude model ($k = 0$ and $\omega_0 = 0$) and the midinfrared component is fit to Lorentz oscillators with $k > 0$. Here, we assigned the MIR optical process to the
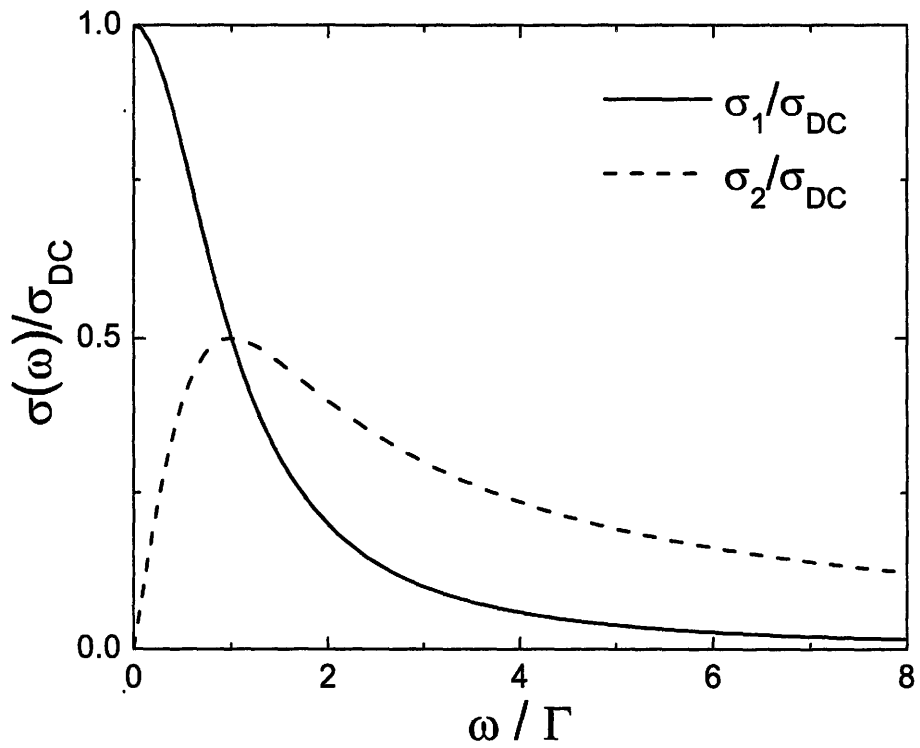
Figure 2.1 The relative real and imaginary parts of the optical conductivity as functions of (ω/Γ) from the Drude model.

interband transitions, where the energy of the photons equals the energy difference between the empty and filled bands in the electronic structure of the material.

2.3.2   One-component Model : Extended Drude Model

Apart from the Drude-Lorentz analysis, the extended Drude model (Allen, 1971) is an alternative way to study non-Drude optical conductivity of materials, at low frequencies. It considers a single low-frequency contribution of frequency-dependent scattering and effective mass to the dielectric function. The IR conductivity is believed to be the results of the inelastic scattering processes between free electrons and bosonic excitations. In this picture, the usual expression of Drude conductivity becomes,

$$\sigma(\omega, T) = \frac{1}{4\pi} \frac{\omega_p^2}{1/\tau(\omega, T) - i\omega[1 + \lambda(\omega, T)]}. \tag{2.22}$$

where $1/\tau(\omega) = \Gamma(\omega)$, the scattering rate, and $1 + \lambda(\omega) = m^*(\omega)/m$, the radio of the effective mass to the bare electron mass. Thus, the frequency-dependent scattering rate and effective mass can be obtained from the complex optical conductivity. The calculations of $1/\tau(\omega)$ and $m^*(\omega)/m$ by Matlab programmes can be found in Appendix A.

Chapter 3

OPTICAL MEASUREMENTS

3.1   Introduction

In this chapter, the experimental techniques are presented. In Section 3.2, a brief description of the Infrared Fourier transform spectrometer and the setups used to obtain data over a wide frequency range are introduced. In the following section, 3.3, we talk about important techniques adopted to obtain the more accurate reflectance data. In the end, compared with previous experiment systems, the improvements of the current system will be explained in Section 3.4.

3.2   Spectrometer and Setups

A commercial Bruker IFS 66v/S spectrometer, which is a IR Fourier transform spectrometer, was used to measure the reflectance of the $Nd_{1-x}TiO_3$ system. It consists of an interferometer compartment, which generates the incident light, several mirrors for focusing and reflecting beams, a sample chamber and a detector. The interferometer compartment mainly contains a light source, an aperture, a beam

splitter, a fixed mirror and a moving mirror. The configuration of the instrument is shown in the schematic diagram in Figure 3.1. The part of evaporator apparatus (M) will be discussed in Section 3.3.2.

The interferometer compartment is essentially a Michelson interferometer. The beam of light from the source is split by the beam splitter and then the split beams are combined after being reflected from the fixed (E) and moving mirror (H). The difference in the lengths of the light paths of the two split beams determines the phase difference between the two beams and the phase difference gives rise to an interference pattern. As a result, the intensity of the combined beam as a function of path length difference is called interferogram. The interferogram can be Fourier transformed to the intensity as a function of the frequency of light, which is a single power spectrum. After being reflected from several mirrors, the combined beam projects onto and is reflected from the surface of the sample or the reference mirror (N). Finally, the reflected beam is focused on the detector (O) and the program, we used, takes Fourier transform of the interferogram from the detector and produces the power spectrum.

The nearly normal-incident reflectance of the sample can be measured from 50 cm^{-1} up to 40 000 cm^{-1} by the spectrometer. In order to obtain the reflectance data over this wide frequency range, 4 combinations of source, beam splitter, window and detector were used in the experiments as listed in Table 3.1.

3.3   Experimental Details

3.3.1   The *In Situ* Evaporation Technique

We applied an *in situ* evaporation technique (Homes et al., 1993) to correct geometrical effects from an irregular surface. Before the evaporation, we take the
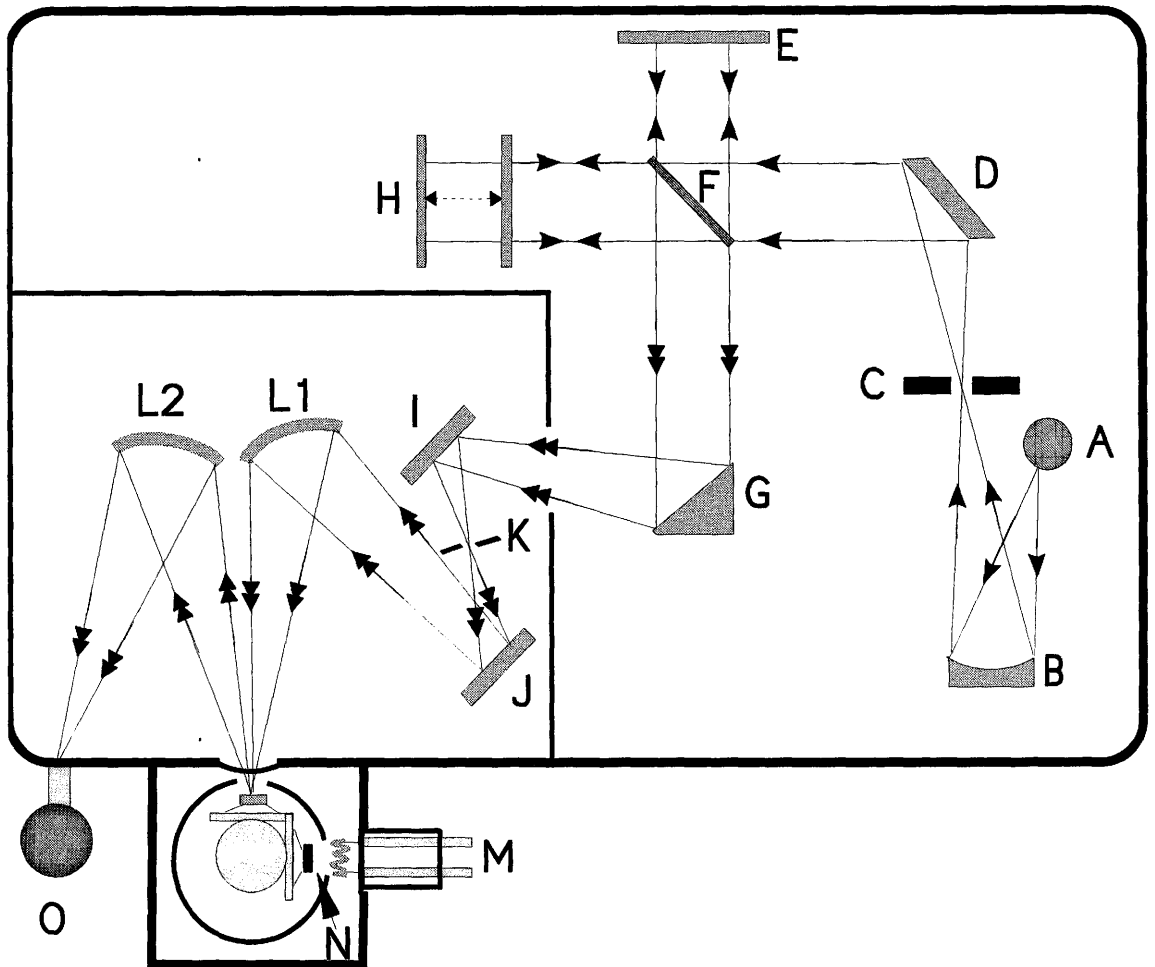
Figure 3.1 Schematic diagram of the Fourier transform spectrometer: (A) light source; (B)concave mirror; (C) aperture; (D) concave mirror; (E) fixed plane mirror; (F) beam splitter; (G) concave mirror; (H) moving plane mirror; (I,J) plane mirror; (K) aperture; (L1,L2) toroidal mirror; (M) evaporator apparatus; (N) sample or reference mirror; (O) detector.

power spectra of reference mirror (R_r) and sample (R_s) in succession and calculate the radio (R_s/R_r). After all the radios at different temperatures have been obtained, we evaporate a layer of Au or Al onto the sample surface. The evaporator apparatus (M) contains two electrodes and one tungsten filament connected between them. Three pieces of gold or aluminum, each of which is $\sim$ 7mm in length, are hung on the W filament. The current is increased slowly to 2 A and kept for a few seconds until the pieces of gold are melted and wet the W filament. We further increase the current to 4 A and wait for about 10 seconds to evaporate the gold onto the sample surface. The layer of gold is thick enough to avoid multiple reflection from the sample-gold interface. The evaporation was carried out under $\sim 10^{-6}$ Torr at room temperature 300 K. The reflectance of the reference mirror and the coated sample were taken again and the radio of them (R_g/R_r) was obtained. The absolute value of the reflectance of the sample can be calculated by the relation:

$$R_s^{abs} = (\frac{R_s/R_r}{R_g/R_r}) \times R_g^{abs} \qquad (3.1)$$

Table 3.1 Combination of source, beam splitter, window and detector used for 4 different frequency ranges.

Frequency	Light Source	Beam Splitter	Window	Detector
Far IR (50-650 cm^{-1})	Hg arc lamp	6 μm Ge/Mylar	Polypropylene	4K Bolometer
Mid IR (400-6000 cm^{-1})	Globar	Ge/KBr	KBr	MCT (77K)
Near IR (3000-14 000 cm^{-1})	W lamp	UV/Ca	KBr	MCT (77K)
NIR,VIS,UV (12 000-45 000 cm^{-1})	D$_2$ lamp	UV/Ca	KBr	PMT

where R_g^{abs} is the absolute reflectance of gold. We estimate the absolute accuracy of the reflectance to be better than $\pm$ 0.5 %.

For the fourth frequency range in Table 3.1, 12 000 cm^{-1} to 45 000 cm^{-1}, we evaporated aluminum onto the surface of sample, for the reflectance of gold reduces by 60 % above yellow frequency.

3.3.2 Extrapolations

As mentioned in Section 2.2.2, the Kramers-Kronig (KK)analysis used to get the phase factor θ from the reflectance requires that the value of reflectance from zero-frequency up to infinity be known. However, in reality, we can only do the measurements over a finite frequency range. Consequently, an extension of the reflectance data beyond the frequency region in our study would be needed. The low-frequency reflectance was extrapolated toward zero frequency by the Hagen-Rubens approximation (see Appendix B), $R(\omega) = 1 - A\sqrt{\omega}$, for the metallic sample ($x = 0.095$). A is the only parameter in the approximation and the programme[1], we used, takes the point corresponding to the lowest frequency to calculate A and then use the Hagen-Rubens relations to get the low-frequency extrapolation curves. This procedure can produce non-smooth extrapolation if the low-frequency data are too noisy. However, our data are relatively noisy free at low frequencies and the Hagen-Rubens extrapolation curve follows the whole data curve rather well. For the two insulating and semiconducting samples, the reflectance is assumed to be constant towards DC for the low-frequency extrapolation. At high frequencies we employed the reflectance data of BaTiO$_3$ (Kolodiazhnyi et al., 2004) between 40 000 and 100 000 cm^{-1} for all the three samples and assumed a free carrier response, $R = \omega^{-4}$, beyond 100 000

---

[1]The programme for performing KK transformation, KK.exe, was written by C. D. Porter and supplied to us by the group of D. B. Tanner of the University of Florida in Gainesville.

cm^{-1}. The adoption of the data of $BaTiO_3$ is reasonable, since there is no big change in the reflectance of titanates in the near-infrared region (Crandles et al., 1992) and a small shift of high-frequency reflectance won't affect the optical conductivity spectra below 10 000 cm^{-1}.

3.3.3 Experimental Procedures

The optical experiments were performed on well polished surface of the $Nd_{1-x}TiO_3$ system, around 2×2 mm^2 in size. To obtain the reflectance data at six different temperatures over the wide frequency region, we repeat the same experiment procedure at the four different frequency ranges as listed in Table 3.1. The main experiment procedure contains 5 steps as following:

1. At room temperature, we took 5 sets of radio (R_s/R_r) as mentioned in Section 3.3.1 and averaged them to get $(R_s/R_r)_{300K}$.

2. Decrease the temperature to 28K and repeat the measurements as in step 1 to get $(R_s/R_r)_{28K}$.

3. Increase the temperature and repeat the measurements as in step 1 at different desired temperatures and get $(R_s/R_r)_T$. When approaching the room temperature, repeat step 1 and compare the two sets of results of before and after temperature variation to check if the data difference is within 0.5 %. In this way, we can monitor the variation of the sample surface properties with changes of temperature.

4. Rotate the sample stage to make the sample face to the evaporator apparatus (M). Evaporate Au or Al onto the sample surface as introduced in Section 3.3.1. Repeat steps 1 and 2 to get $(R_g/R_r)_T$.

5. Finally, plug the known quantities $(R_s/R_r)_T$ and $(R_g/R_r)_T$ into Equation 3.1 and get the absolute reflectance of sample at different temperatures, $R_{s,T}^{abs}$.

3.4 Improvements

3.4.1 The Cryostat

The reflectance measurements were performed at six different temperatures, from 28 K to room temperature, 295 K. To minimize movement of the sample due to thermal expansion, the sample stage is not attached directly to the cryostat as in previous work. As shown in Figure 3.2, the sample stage is connected by a flexible silver foil band to a continuous ^{4}He flow cryostat (R. G. Hansen & Associate). In order to isolate the sample stage from room temperature, the sample stage is fixed to the ambient temperature stainless steel block by three quartz rods. Silicon wafers are inserted between the interfaces of the stage and the rods to avoid enlargement of the interface which would cause more heat transfer. One nylon screw is used to pull the stage down onto the rods to stabilize the heavy stage. We also put several layers of super-insulation between the stage and the stainless steel block to reduce the room temperature radiation. To obtain the required temperature for measurements, we control the flow of the liquid ^{4}He and use a temperature controller (Lakeshore 330) to monitor and stabilize the temperature of the sample stage. The whole configuration guarantees a lowest temperature of 20 K for the sample.

3.4.2 Automatic Measurements

Many experiments have been done with the previous infrared system in our laboratory. The new instruments for optical study represents a big improvement over
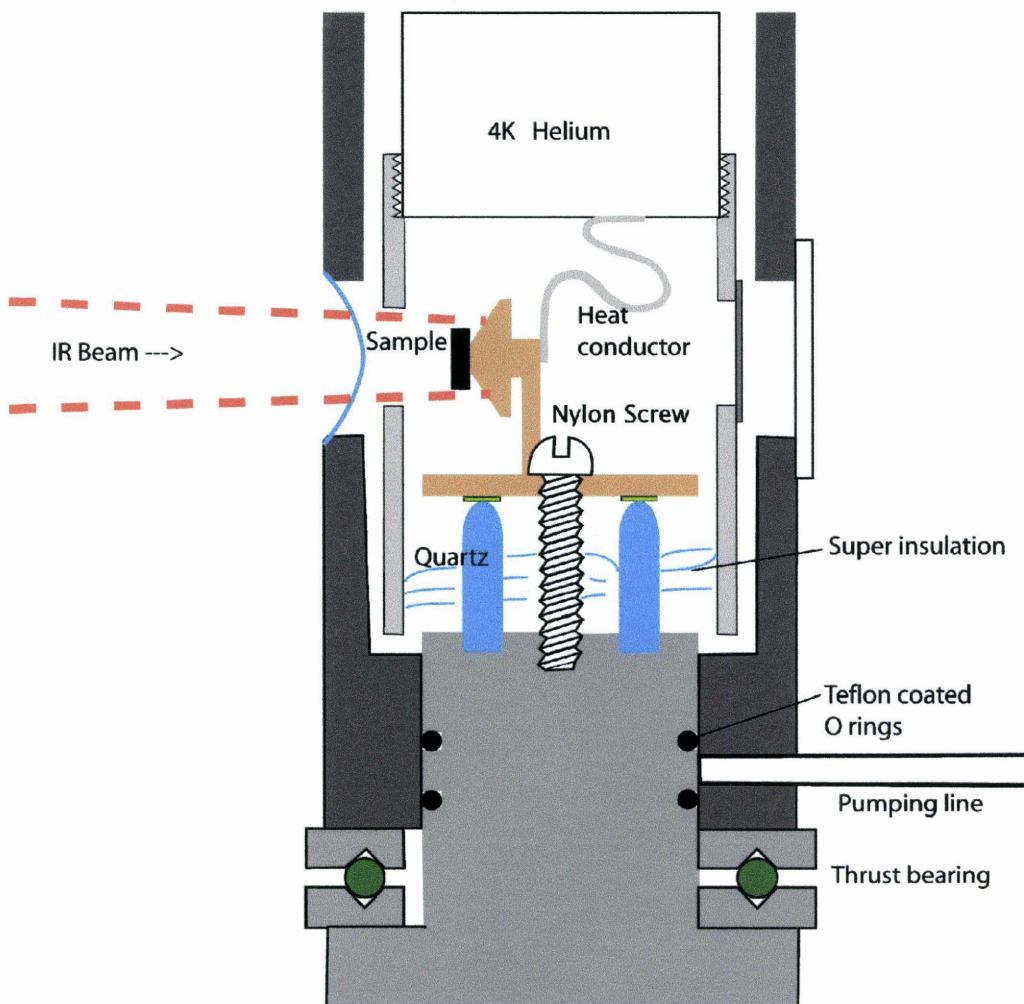
Figure 3.2 Sketch of the sample stage and its connections to the ^{4}He flow cryostat and the ambient temperature stainless steel block.

the previous system. Instead of manually carrying out experiments as in the past, we introduced a new automated control system (developed by the Intelliscience Instrumentation ·Inc.) to the current spectrometer. In the new system, the control of temperatures, the rotation of the sample stage to the proper position and the taking of several sets of data at each temperature can be done automatically. Figure 3.3 schematically illustrates the configuration of the automated control system. The LabView program is the central operator of the whole control system. To control the temperature of the cryostat, the LabView program tells the ^{4}He flow controller to control gas flow with the assistance of the breakout box, and sets the parameters of the temperature controller which monitors the cryostat temperature and starts the cryostat heater 1 when necessary. After the stable desired temperature has been reached, the LabView program will ask the breakout box to check if the sample stage is located at the proper position (reference or sample) for measurements, via two sample pads that are connected to the sample stage arm and have electrical contact with the sample stage set screws. If the position of the sample stage is improper, the LabView program will start the stepper motor through the stepper motor controller to rotate the sample stage to the proper position. When the sample stage has been rotated to the sample or reference position, the LabView program will tell the Bruker computer to take data. The actual appearance and arrangement of the automated control system in the current experiments are shown in Figure 3.4.

·
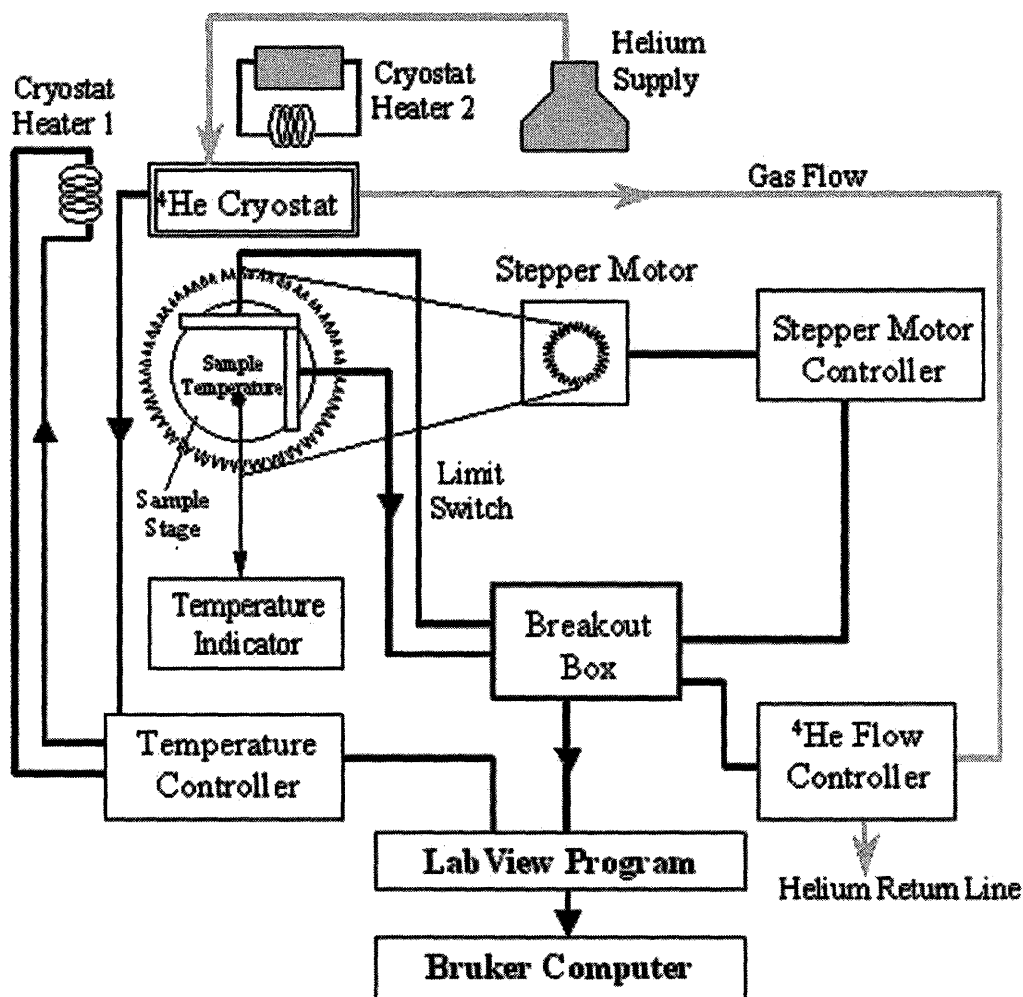
Figure 3.3 The schematic diagram of the automated control system. The black thick lines show how the electronic components are connected. The grey arrows indicate the direction of the helium flow. The cryostat heater 2 on the top of the ^{4}He cryostat is in another control and for protecting the O rings from the low temperature.
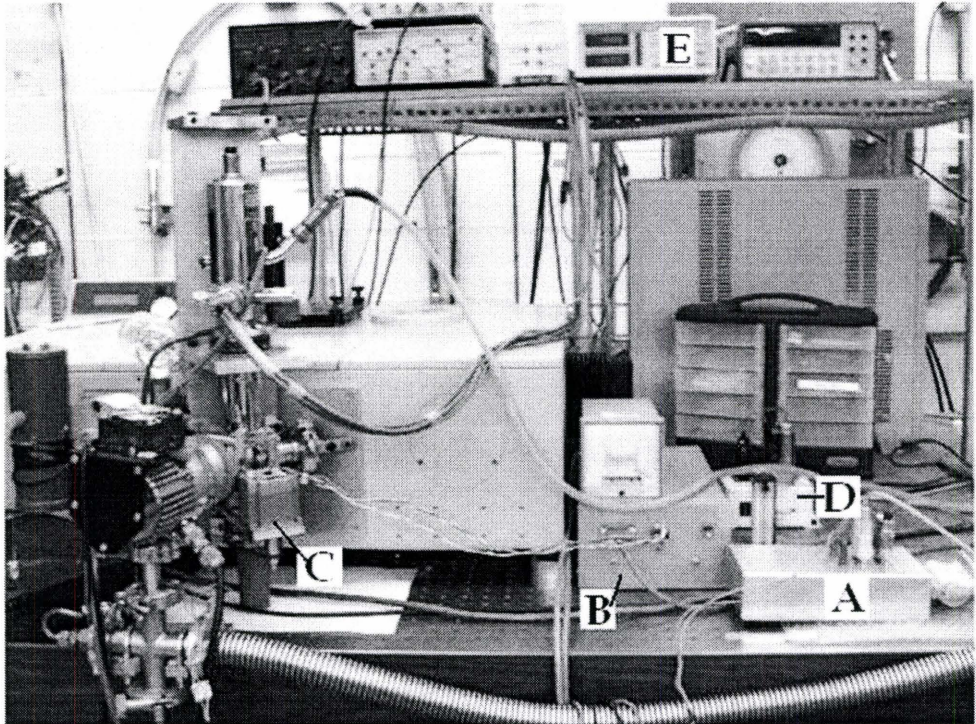
Figure 3.4 The hardware of the automated control system and related connections: (A) the breakout box; (B) the stepper motor controller; (C) the stepper motor and the stepper motor mount; (D) the flow controller; (E) the temperature controller. The barometer standing between the cryostat helium exhaust and the flow controller input is for monitoring the helium flow changes.

Chapter 4

RESULTS AND DISCUSSION

4.1 Introduction

We present the results of the optical measurements of the $Nd_{1-x}TiO_3$ system in this chapter. As mentioned in previous chapters, the samples are single crystals at three doping levels, $x = 0.019, 0.046$ and 0.095 and the IR spectroscopy was taken at six different temperatures, 28 K, 51 K, 101 K, 201 K, 247 K and 295 K, respectively. Since the samples are 3D perovskites, a polarized incident light or the consideration of the sample orientation is not needed in the current study. We analyzed the data in terms of doping-dependent and temperature-dependent optical properties respectively and the results and discussions are presented in Section 4.2 and 4.3.

4.2 Hole-doping-dependent Optical Properties

4.2.1 Reflectance and Optical Conductivity

Figure 4.1 presents the room-temperature reflectance of $Nd_{1-x}TiO_3$ at three doping levels, $x = 0.019, 0.046$ and 0.095, within the frequency region below the highest frequency of our study. The data show typical behavior of metal, semiconductor and insulator, respectively. The reflectance of the metallic sample is close to unity at low frequencies and descends quickly to a minimum around 10 000 cm^{-1}. The insulator exhibits sharp phonon peaks at low frequencies and the reflectance reaches almost zero at frequency right above the phonons. While the semiconducting sample displays a in-between behavior of the first two samples. The upturn around 40 000 cm^{-1} in all the three samples is assigned to the interband transition which will be discussed in details later based on the conductivity spectra . The existence of three main sharp phonons, observed in the insulating and semiconducting samples in the far-infrared region, are consistent with the prediction of group theory for cubic perovskites. The small splittings in the second phonon mode, as seen in the insulating sample, originates from the orthorhombic distortion in the cubic structure (Crandles et al., 1994). The phonon modes are weaken in the reflectance of the metallic sample.

By Kramers-Kronig transformation of the reflectance, we obtained the real part of the optical conductivity at room temperature at three doping levels in Figure 4.2(a). The spectrum of the insulator consists of two separated electronic-absorption processes. Two gaplike features can be recognized easily around 10 000 cm^{-1} and 30 000 cm^{-1}. The spectral weight of the low-frequency plateau has been distributed to the Mott-Hubbard (MH) transition between the lower (LH) and upper Hubbard (UH) bands and the rapid increasing of spectral weight above 30 000 cm^{-1} the charge-transfer (CT) transition from the filled O $2p$ states to the empty LH band (Arima
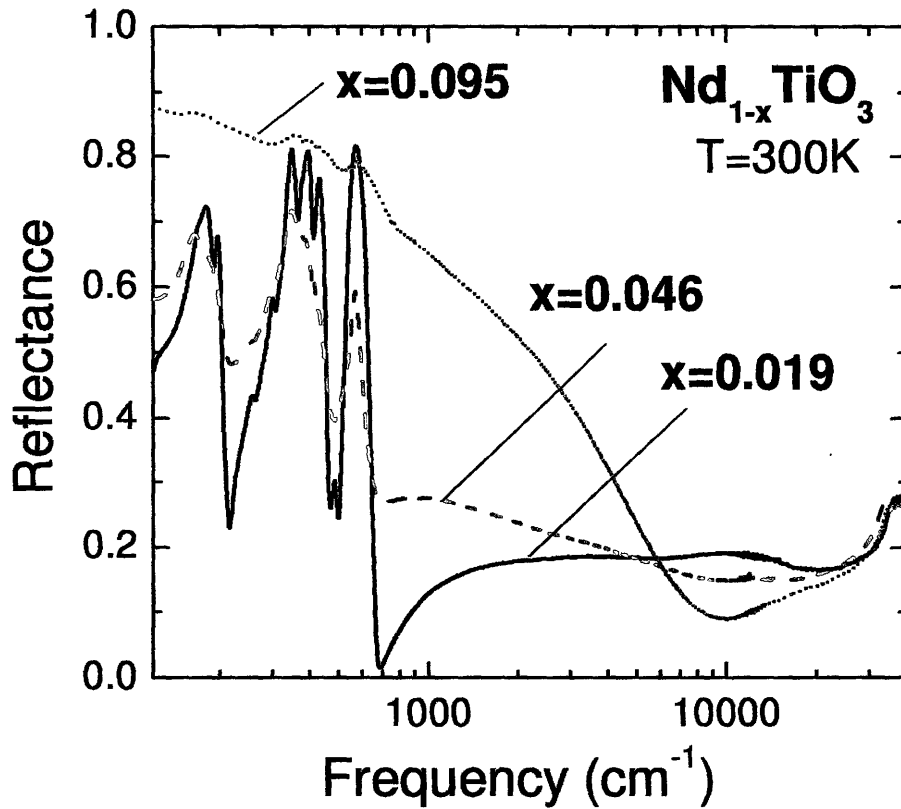
Figure 4.1 The reflectance of $Nd_{1-x}TiO_3$ at three doping levels, at room temperature. To clarify the structure of the spectra, the frequency axis has a logarithmic scale. $x = 0.095$ shows metallic behavior, while $x = 0.046$ and 0.019 show typical optical spectra of a semiconductor and an insulator, respectively.
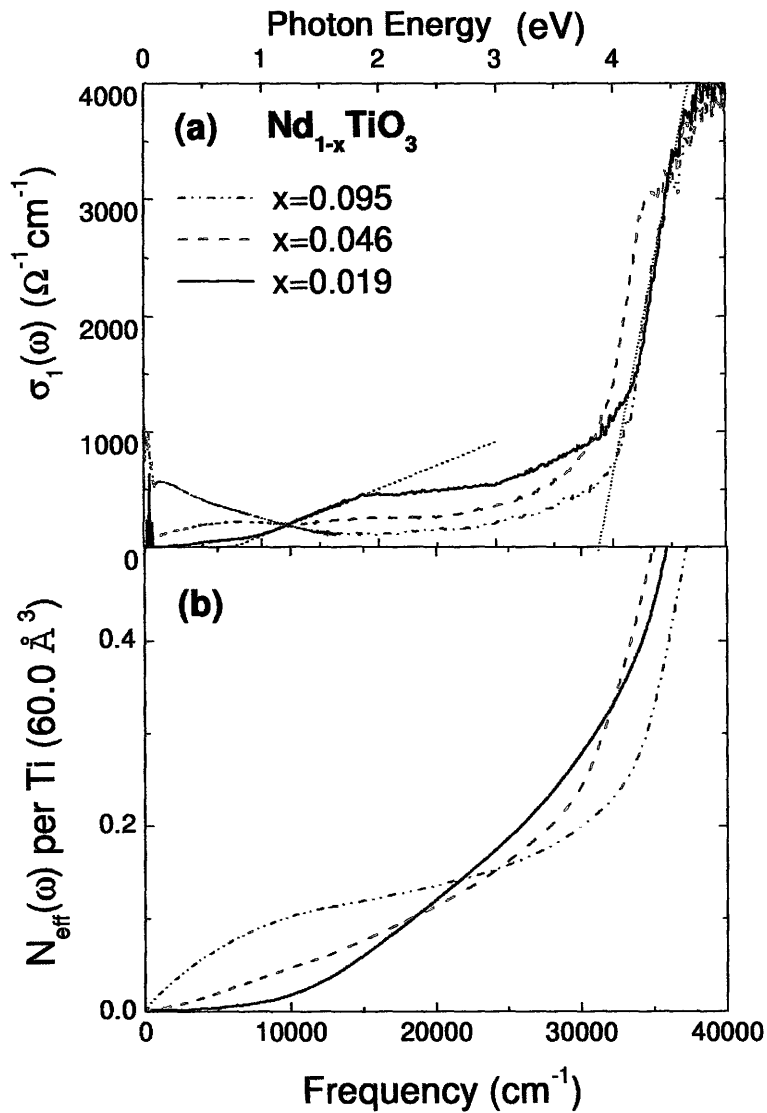
Figure 4.2 (a) The optical conductivity spectra of the three samples at room temperature. Dashed lines show the linear extrapolation of the edge of the MH and CT transitions. (b) The effective electron number per Ti site, or partial spectral weight, as a function of frequency at three doping levels. $N_{eff}(\omega)$ is calculated by the integration in Equation 2.14 with V_{Ti}=60.0 $\AA^3$ (Sefat, 2005).
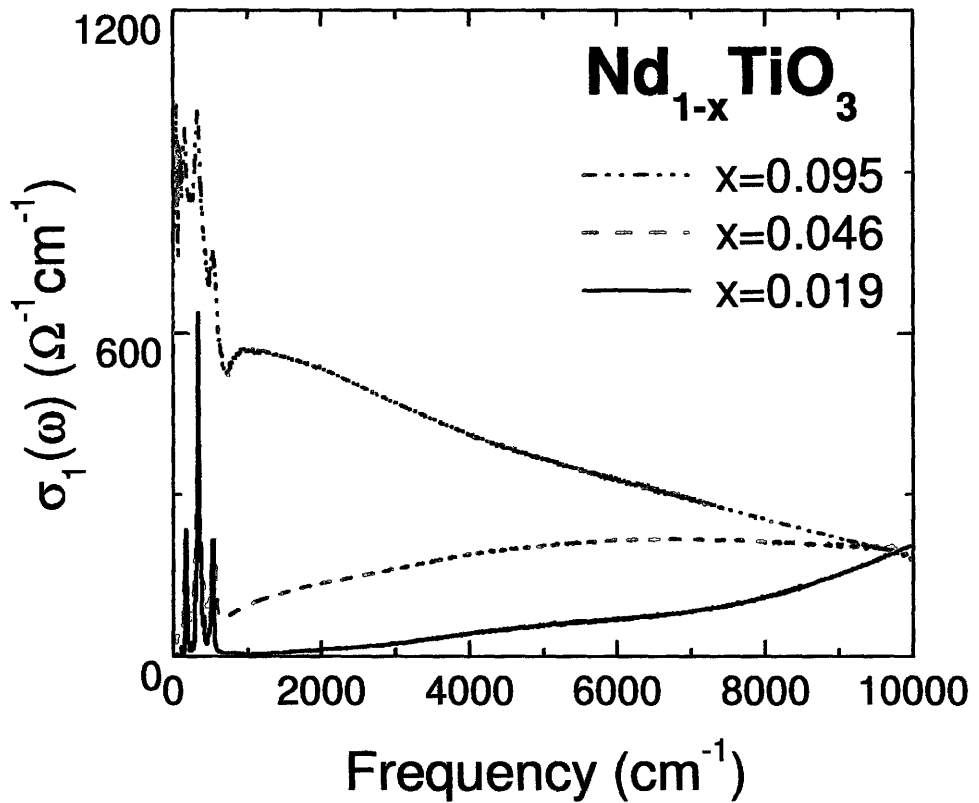
Figure 4.3 The expanded view of the low-frequency optical conductivity of the three samples at room temperature.

et al., 1993) as shown in Figure 4.4 (a). We estimated the onsets of the two transitions, $U - W$ and $U - W/2 - W'/2$, to be $\sim$0.8 eV and $\sim$4 eV respectively from the intersection points of the extrapolated linear fits to the transition edge and the abscissa, in accord with previous studies (Arima et al., 1993, Katsufuji et al., 1995). The remnant spectral weight below 0.8 eV is due to a slight Nd nonstoichiometry, $x = 0.019$ as shown by neutron observation (Sefat, 2005). The relative position of the two gap excitations suggests that the insulating d^1 (Ti^{3+}) compound is a Mott-type insulator rather than a CT insulator in the Zaanen-Sawatsky-Allen (ZSA) scheme (Zaanen et al., 1985).

As the hole doping proceeds, the spectral weight of the MH transition decreases, whereas that below the onset frequency of the MH transition increases monotonically, as seen in the doped samples in Figure 4.2(a). As seen in Figure 4.3, the excitations within the original gap region contain a Drude absorption peak and a broad midinfrared (MIR) absorption. Meanwhile, the center frequency of the midinfrared band seems to move to lower frequencies as hole concentration increases. Similar behavior has been seen in the $R_{1-x}Ca_xTiO_3$ system (Katsufuji et al., 1995).

4.2.2   Analysis and Discussion

The doping-dependent low-frequency conductivity of $Nd_{1-x}TiO_3$ resembles that of the superconducting cuprate $La_{2-x}Sr_xCuO_4$ (Uchida et al., 1991) with a midinfrared absorption that grows and moves to lower frequencies with hole doping. Another similarity is an isosbestic point, where conductivity curves across, presents in both systems. The spectral weight lost above this point, $\sim$1.2 eV in $Nd_{1-x}TiO_3$, moves to the region below it and the spectral weight is conserved around 3 eV, below the onset frequency of the CT transition, as shown in Figure 4.2(b). Namely,

spectral weight is transferred from MH excitations to the Drude and MIR excitations with doping. The transfer of spectral weight from high-frequency region to the low-frequency part with doping is actually a general feature of strongly correlated systems (Eskes et al., 1991). However, it is interesting to note that in the Na_xCoO_2 system, no spectral weight transfer was seen from the high-energy transitions to the Drude and MIR parts as hole concentration increases (Hwang et al., 2005a). The differences between LSCO and the titanate system is also notable. In LSCO the midinfrared peak evolves into the Drude component eventually, above certain doping level, and the CT gap excitations persist in the metallic samples. Whereas, in the current titanate system, the optical conductivity related to the MH excitations are quite low at high doping levels. Besides, the midinfrared peak still exists in the sample of the highest doping level of our study. Study on the spectra of highly doped titanates are needed to conclude that if the midinfrared peak will finally be merged into the Drude peak or not.

As mentioned in Section 2.3, the infrared conductivity spectra can be explained within two-component or one-component models. Here, we talk about the two-component model first and the other model will be discussed in Section 4.3.2. Considering two-component model, the features in infrared conductivity spectra discussed above can be partially accounted for by the proposed schematic electronic structure of hole-doped $Nd_{1-x}TiO_3$ as shown in Figure 4.4. Upon hole doping, a small portion of spectral weight is transferred from the lower Hubbard band to a broad so-called mid-gap band inside the Mott gap, above E_F, in the slightly-doped insulating sample. As the hold doping proceeds, the spectral weight is further transferred to a second sharper mid-gap band, located below the first mid-gap band and above E_F in the semiconducting and metallic samples. In the metallic phase, there is quasi-particle spectral weight at E_F in the LH band. Now let's compare the proposed
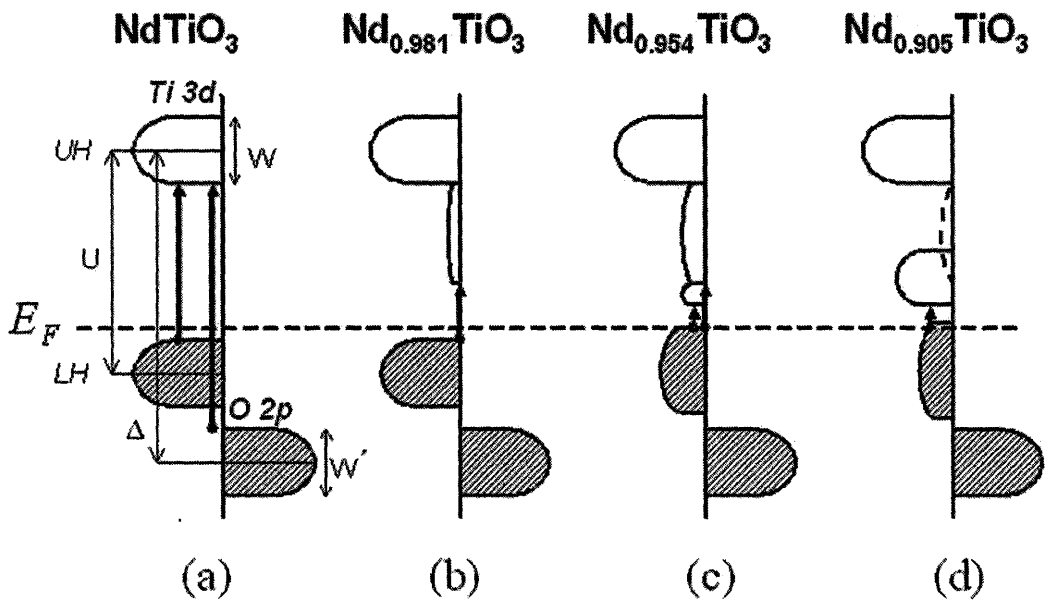
Figure 4.4 Schematic electronic structure of undoped (a) and hole-doped (b,c,d) $Nd_{1-x}TiO_3$. With hole doping, the spectral weight is transferred from the lower Hubbard band to the mid-gap bands, developing inside the Hubbard gap. The arrows represent the onset frequencies of the transitions and they are plot in scales based on the spectra in Figure 4.5.

electronic structure to the experimental results at 28 K shown in Figure 4.5. The broad absorption with the onset energy of 1 000 cm^{-1} and below the Mott transition in the insulating sample as well as the broad absorption peak P2 in the semiconducting sample can be assigned to the transitions from the LH band to the broad mid-gap band in Figure 4.4 (b) and (c). The sharper absorption peak P1 in the semiconducting sample and the one around 2 000 cm^{-1} in the metallic sample correspond to the transitions from the LH band to the sharper mid-gap band in Figure 4.4 (c) and (d). Figure 4.4 (d) shows that the two mid-gap bands overlap which is consistent with the conductivity spectrum of the metallic sample in Figure 4.5 where we cannot resolve the second absorption peak corresponding to P2. Besides, since the spectral weight around 9 000 cm^{-1} is lower than that in the semiconducting sample, the broader mid-gap band in Figure 4.4 (d) is shown with dashes to illustrate the possibility that the band may disappear in the metallic sample. The growing of the spectral weight of the mid-gap states and the reduction of the LH band with hole doping explains why the spectral weight is transferred from MH excitations to the MIR excitations below the Mott transition in the optical conductivity spectra with increasing doping levels. The Drude peak in the metallic sample is due to the quasi-particle spectral weight at E_F in the LH band. We lack photoemission (PES) or inverse photoemission spectra (BIS) data for the current system to verify the proposed schematic electronic structure, however, this picture is in good agreement with the existent PES, BIS and x-ray-absorption data of other hole-doped titanium oxides (Morikawa et al., 1996, Fujimori, 1992, Robey et al., 1995, Yokoya et al., 1999). What is different from those results in our study is that in the doped samples the mid-gap state doesn't occupy the whole Hubbard gap and a small gap remains above the Fermi surface, as seen in Figure 4.4 (b), (c) and (d). In other words, the quasi-particle spectral weight at E_F is only from the LH band in the weakly doped metal. We identified the small

gap in our optical spectra by subtracting the phonon and Drude contributions from the conductivity of $Nd_{0.905}TiO_3$ and removing the phonons only from $Nd_{0.981}TiO_3$ and $Nd_{0.954}TiO_3$ at the lowest temperature as shown in Figure 4.5. The curves of the doped samples demonstrate clearly non-zero intersections with the abscissa, which can be considered as the onset frequency of the transition from LH band to the mid-gap states in Figure 4.4(b), (c) and (d). Further study of metallic samples at higher doping levels are necessary to see if the small gap will vanish or not, or if the top of LH band and the bottom of the mid-gap band will coalesce or not, with doping.

Although the origin of the formation of the mid-gap state is not clear yet, we can quantitatively analyze the evolution rate of the Drude and MIR excitations, namely, the excitations related to the mid-gap state, with doping, based on the proposed electronic structure in Figure 4.4. That is also the rate of the spectral weight transfer from the MH excitations to the frequencies below the MH-transition energy respect to doping. Here we adopted the procedure performed in an earlier study by Katsufuji et al. (1995) and present our results in Figure 4.6. $N_D = N_{eff}(\omega_c)_p - N_{eff}(\omega_c)_{p=0}$, where $N_{eff}(\omega_c)_p$ is the effective electron number associated with the Drude and the MIR absorptions below the isosbestic point ($\omega_c \sim 1.2$ eV) at different doping levels (p), consequently, N_D represents the spectral weight transferred from the spectrum above ω_c, the MH excitations, to that below ω_c as a function of doping p. Figure 4.6 illustrates N_D increases approximately linearly with the hole concentration with a slope of $N_D/p = 0.37$. The quantity N_D/p is called the spectral weight transfer rate. Previous spectroscopic studies (Katsufuji et al., 1995) gave a transfer rate of 0.31 ± 0.07 for another titanate system, $Nd_{1-x}Ca_xTiO_3$. Within the systematic uncertainties of our study, the two systems have consistent transfer rate. Note that these two systems have the same parent compound $NdTiO_3$. According to previous studies (Katsufuji et al., 1995, Okimoto et al., 1995), the rate of spectral
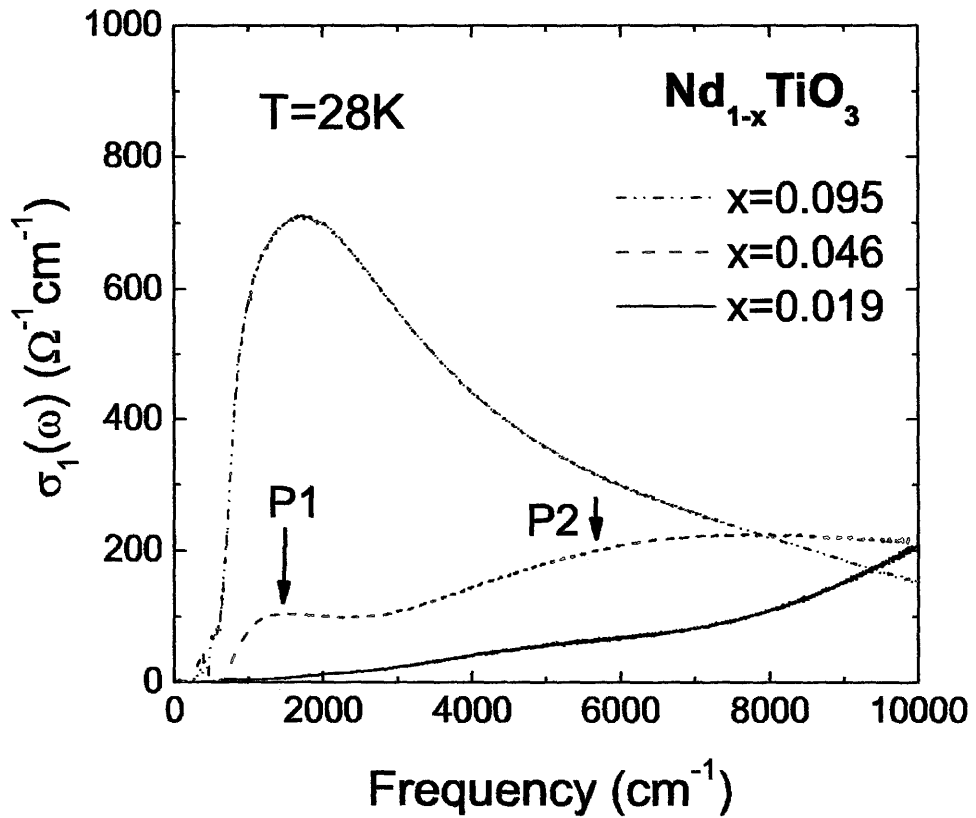
Figure 4.5 Expanded view of the lowest charge gaps at 28 K at different doping levels. To display the evolution of the mid-gap state clearly, we removed the Drude band and the phonon contribution from the metallic sample and phonons from the semiconducting and insulating samples.
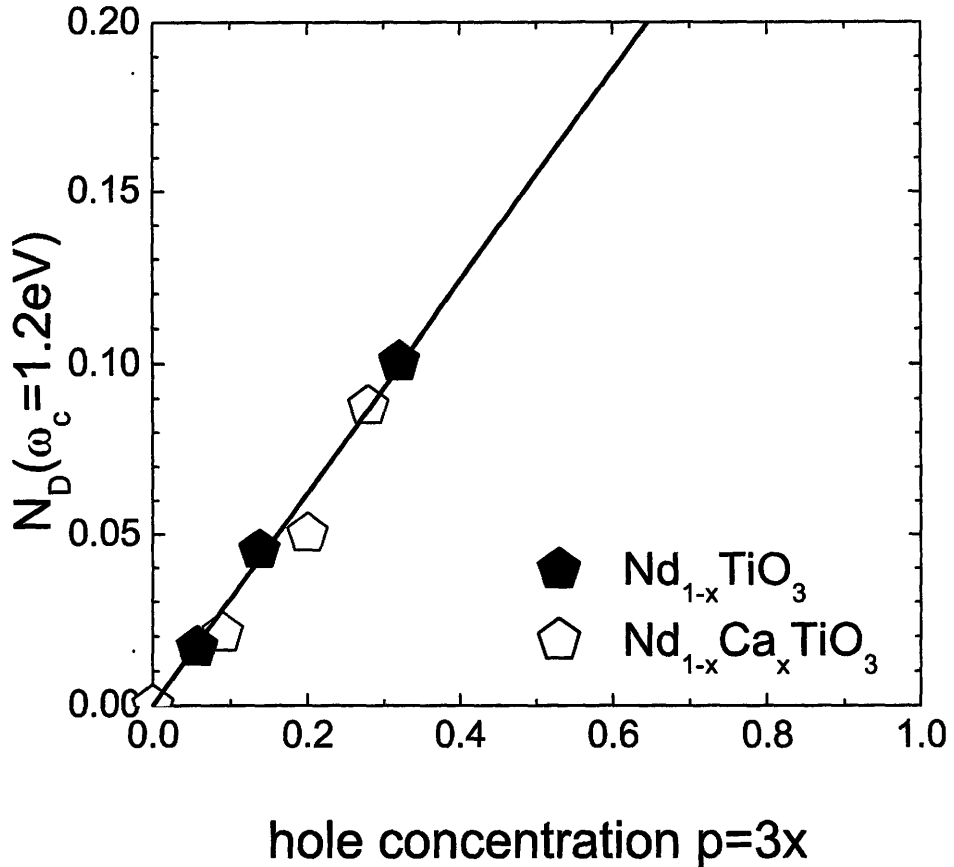
Figure 4.6 Effective electron number related to the Drude and MIR excitations as a function of hole concentration p. The closed pentagons are our results of $Nd_{1-x}TiO_3$ and the open ones are for $Nd_{1-x}Ca_xTiO_3$ from previous studies (Katsufuji et al., 1995). The straight line is a least-squares fit to our data.

weight transfer with doping of various series of titanate is a linear function in terms of the electron correlation strength (U/W) of the corresponding parent insulator. Our optical study of the current titanate system confirms this conclusion since doped samples with Nd vacancies, instead of substitution of Ca for Nd, gave a consistent result with the latter and they both have the same parent insulator $NdTiO_3$.

4.3 Temperature-dependent Optical Properties

4.3.1 The Conductivity Anomaly

In Figure 4.7, we display the temperature dependent reflectance of the correlated metal $Nd_{0.905}TiO_3$. The reflectance, below 7 000 cm^{-1}, increases monotonically as the temperature is lowered from room temperature to 28 K. However, this behavior is reversed above 7 000 cm^{-1}.

Figure 4.8 presents the corresponding optical conductivity up to 8 000 cm^{-1}. A comparison between the dc resistivity data and the inverse of the extrapolated dc optical conductivity is shown in Figure 4.9. Although the trends of the two curves quite match, a discrepancy by a factor of 1.3-2 is clearly discernible. The difference may come from the contact geometry of the four-probe resistivity measurements, but is not unexpected because the dc resistivity data is from another piece of sample, although from the same layer, as mentioned in Section 1.3.2. In any case, the parallel trends between the dc transport behavior and the optical results support the reliability of the optical conductivity spectra. The low frequency region of the optical conductivity consists of a narrow Drude absorption peak, coexisting with three phonon peaks, and a broad midinfrared absorption. Note that the optical conductivity up to 5 000 cm^{-1} increases monotonically with decreasing temperatures, whereas,
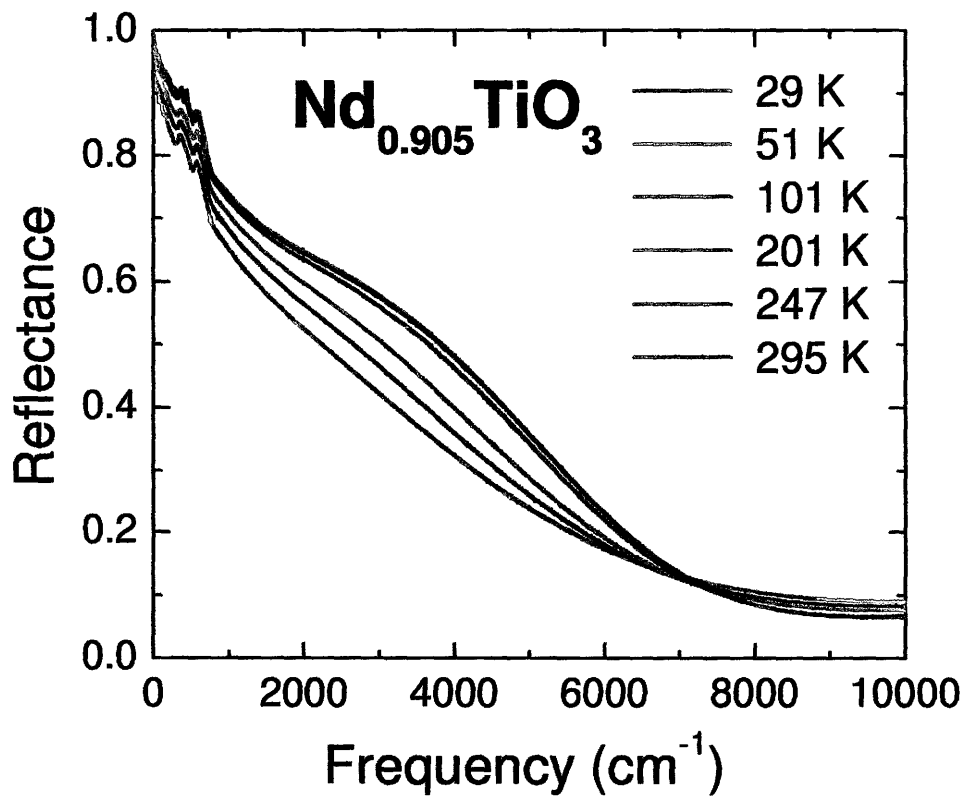
Figure 4.7 Reflectance of the metallic sample $Nd_{0.905}TiO_3$ at different temperatures between 28 K and room temperature.

it decreases above 5 000 cm^{-1}. As introduced in Chapter 2, the f-sum rule implies that the whole spectral weight of materials is not variable with temperature. In Figure 4.10, which demonstrates the partial spectral weight up to 35 000 cm^{-1}, $N_{eff}(\omega)$ increases with decreasing temperature below the frequency around 32 500 cm^{-1} and the difference of the partial spectral weight with temperature goes to zero around 32 500 cm^{-1} except for the curve of 101 K which deviates from the other curves slightly. Both Figure 4.8 and 4.10 tell us that in Nd$_{0.905}$TiO$_3$, the partial spectral weight at 32 500cm^{-1} is temperature independent and as temperature is lowered from room temperature, there is a spectral weight transfer from the region between 5 000 cm^{-1} and 32 500 cm^{-1} to that below 5 000 cm^{-1}. The higher frequency scale corresponds to the onset frequency of the CT transition, as a results of which, the processes of spectral weight transfer happen with excitation energy lower than the CT excitation.

In a recent a-axis optical study of superconducting cuprates, YBa$_2$Cu$_3$O$_{6.50}$ (Tc=59 K), Hwang et al. (2005b) have found similar spectral weight transfer with decreasing temperature in the normal phase. However, in the case of YBCO, the two scales corresponding to the spectral weight transfer with temperature are quite smaller than those in Nd$_{0.905}$TiO$_3$.

The recent article by Ortolani et al. (2005) demonstrated that the temperature dependence of spectral weight $W(\Omega)$,

$$W(\Omega, T) \simeq W_0 - B(\Omega)T^2, \qquad (4.1)$$

holds for conventional metals such as gold and high-T_c superconductors such as BSCCO and LSCO. The spectral weight is a model-independent quantity and defined as:

$$W(\Omega, T) = \int_0^\Omega \sigma_1(\omega, T)d\omega. \qquad (4.2)$$

41
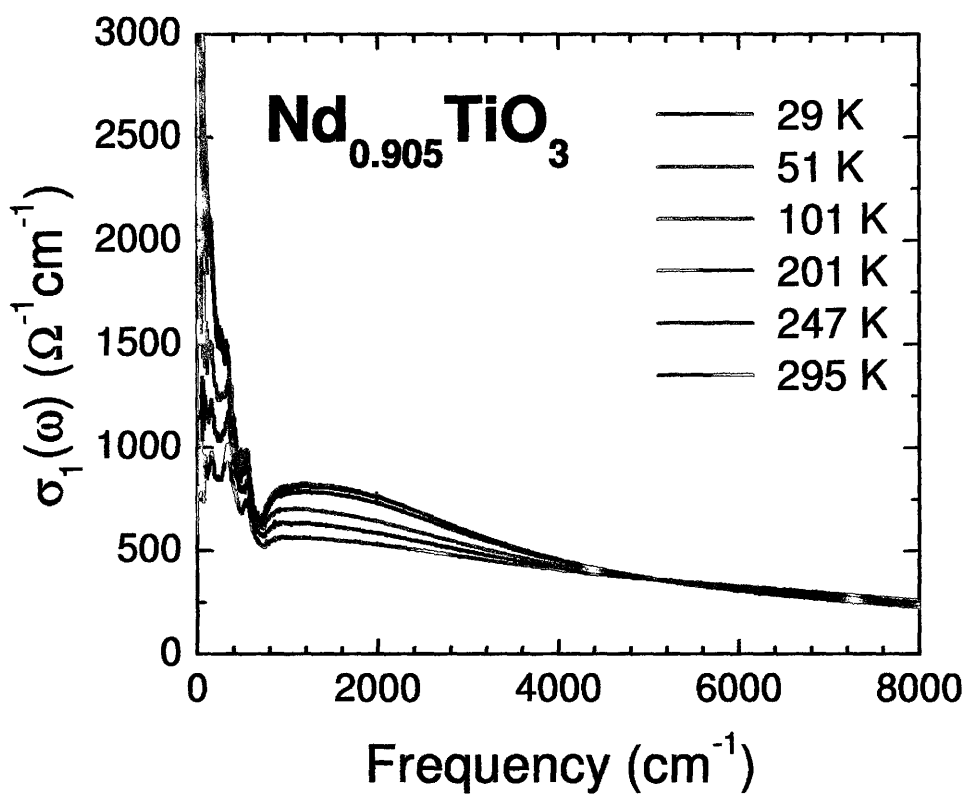
Figure 4.8 Optical conductivity of the metallic sample $Nd_{0.905}TiO_3$ up to 8 000 cm^{-1} at different temperatures between 28 K and room temperature.
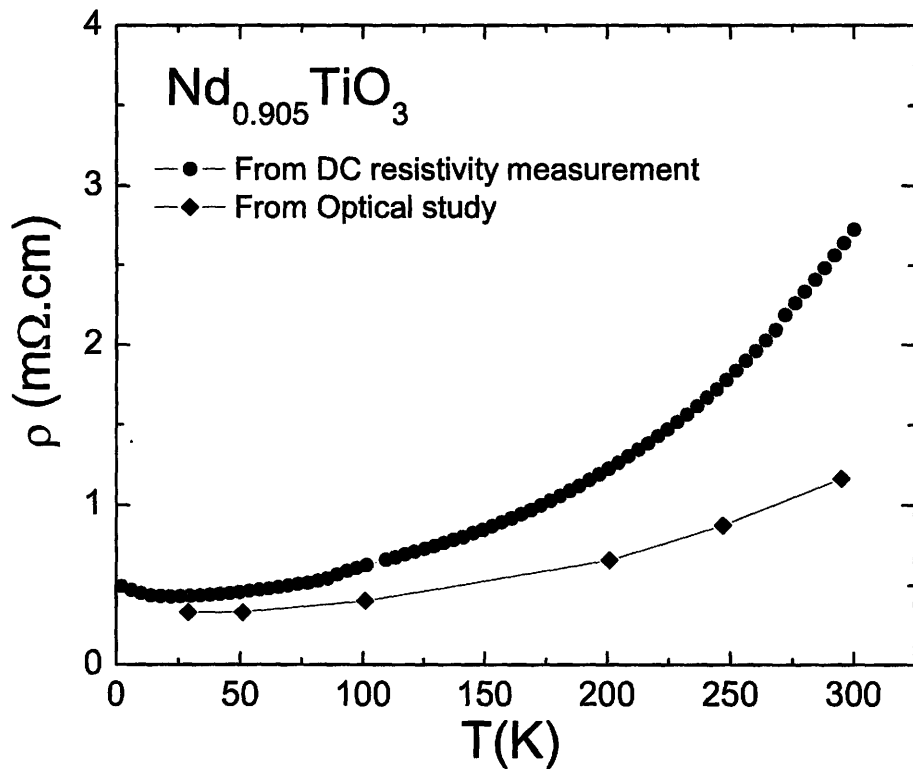
Figure 4.9 DC resistivity data of $Nd_{0.905}TiO_3$ from four-probe measurements and that extrapolated from the optical conductivity spectra at different temperatures.
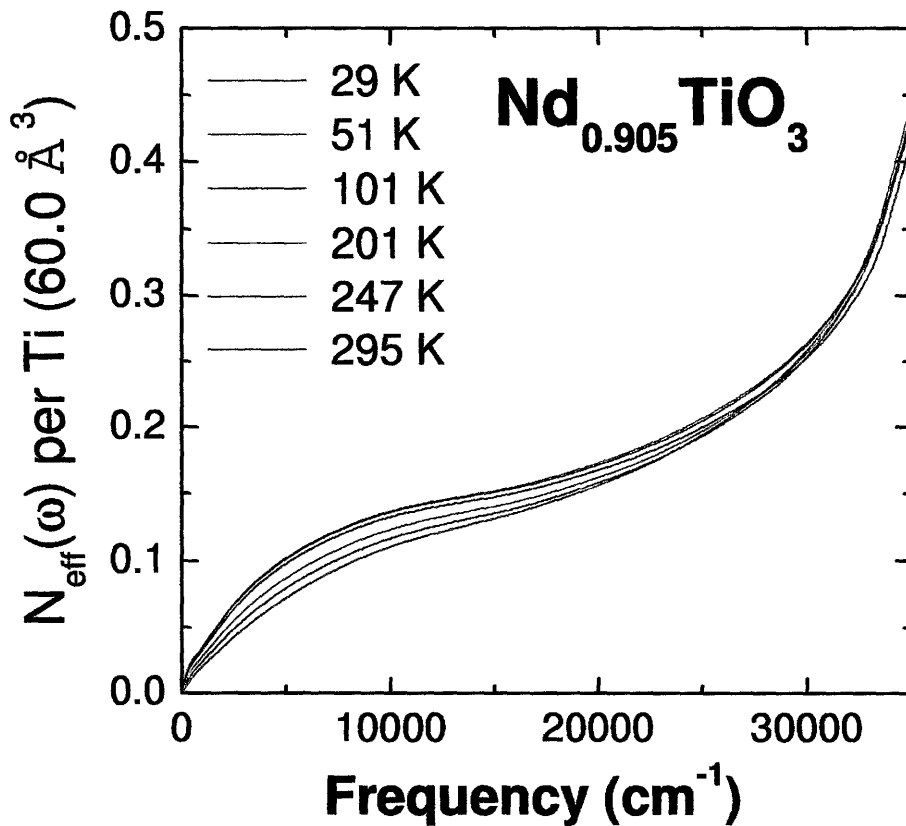
Figure 4.10 The partial spectral weight up to $35\,000$ cm^{-1} of Nd$_{0.905}$TiO$_3$ at different temperatures. The volume per Ti atom is $V_{Ti} = 60.0$ Å^3 .

Equation 4.1 is also verified in $Nd_{0.905}TiO_3$ in our study as shown in Figure 4.11. It should be noted that the choice of high-frequency extrapolation may cause extra uncertainty in the conductivity data above 10 000 cm^{-1} as talked about in Section 3.3.2. Therefore, in Figure 4.11, the data at frequencies above 10 000 cm^{-1} have bigger uncertainties than the rest. For clear illustration, all the data have been normalized to make the intercept on ordinate to be 1. $W(T)/W_0$ with different cutoff frequencies (Ω) decreases linearly with T^2 and the decreasing rate of each linear fit, B/W_0, is Ω-dependent. In Figure 4.12, we display the behavior of $B(\Omega)$ as a function of frequency, which describes the "thermal response" of carriers (Ortolani et al., 2005). The peak around 5 000 cm^{-1} corresponds to the intersection of the conductivity curves in Figure 4.8 and B decreases with frequency above 5 000 cm^{-1} until a minimum 0 around 32 500 cm^{-1}. Meanwhile, B turns to a negative value above 32 500 cm^{-1}, which means the spectral weight increases with temperature at higher frequencies. The behavior of B as a function of frequency is different from that in both gold and LSCO. In Figure 2 of Ortolani et al. (2005)'s paper, all T-dependence of B in gold is below the plasma frequency (ω_p=20 500 cm^{-1}) and $B(\omega_p) = 0$, while in LSCO, the value of B at $\omega_p \simeq 6$ 800 cm^{-1} is nonzero, 1.7 Ω^{-1} cm^{-2} K^{-2}. In our analysis of $Nd_{0.905}TiO_3$, $\omega_p \sim 15$ 000 cm^{-1} and the corresponding value of B is 10 Ω^{-1} cm^{-2} K^{-2}, much larger than that in LSCO.

In discussing of the two-component model, we use Drude-Lorentz oscillators to describe the phonons, the Drude and the midinfrared absorptions in the optical conductivity. Table 4.1 indicates the parameters of the Drude-Lorentz fits to the Drude component and the phonons at different temperatures. Careful readers may raise questions why we didn't list the parameters of the midinfrared oscillators in the table. The midinfrared region shows a hump around 1200 cm^{-1} and a small gap forms right before the hump at all the temperatures, e.g. the case of 28 K in Figure 4.5. As
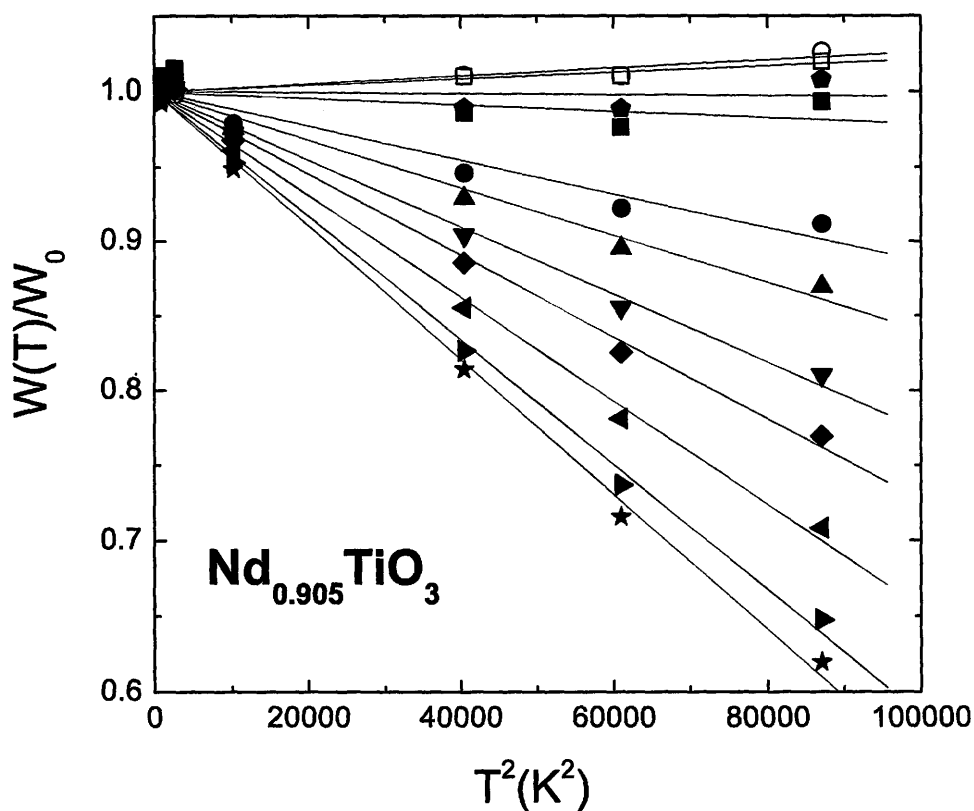
Figure 4.11 Normalized temperature dependence of the spectral weight with different cutoff frequencies in $Nd_{0.905}TiO_3$. The symbols from top to bottom represent data of 40 000 cm^{-1}, 35 020 cm^{-1}, 32 513 cm^{-1}, 30 000 cm^{-1}, 20 000 cm^{-1}, 15 000 cm^{-1}, 10 000 cm^{-1}, 7 500 cm^{-1}, 5 000 cm^{-1}, 3 000 cm^{-1} and 2 000 cm^{-1}, respectively. The straight lines are least-squares fits to the data. For the highest four frequencies, the data at 101 K have been removed before the least-squares fits.
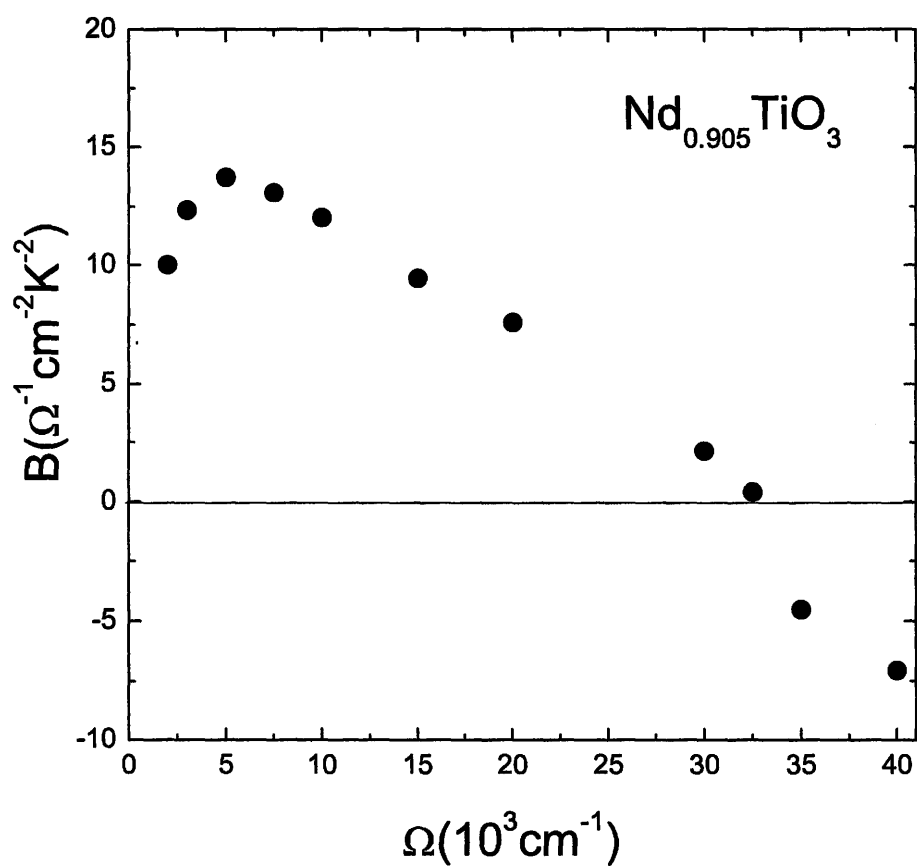
Figure 4.12 The behavior of the coefficient B as a function of frequency in $Nd_{0.905}TiO_3$.

a result, it is hard to fit the midinfrared absorption up to a high frequency, *i.e.* 5000 cm^{-1}, with one or two Lorentz oscillators. Apparently, the second row of the Drude parameters tells the temperature dependence of the scattering rate is consistent with the behavior of free charge carriers in a metal. However, the first row reveals some discrepancy. The increasing of the Drude spectral weight, associated with $\omega_{p,D}$, with decreasing temperature is contrary to the simple fact that the number of free carriers should be a constant respect to temperatures in a metallic sample. Moreover, even without fitting parameters of the midinfrared absorptions, it is obvious from Figure 4.8 that there is a monotonic enhancement of spectral weight with decreasing temperature in the frequency region between 600 and 5000 cm^{-1} in the optical conductivity.

Table 4.1 Parameters of Drude-Lorentz fits at different temperatures for the metallic sample $Nd_{0.905}TiO_3$. For the fits, $\epsilon_\infty = 4.80$. $\omega_{p,D}$ and Γ_D are the plasma frequency and scattering rate of the Drude mode and ω_k, $\omega_{p,k}$ and Γ_k are center frequency, strength and width of the kth Lorentz oscillator.

		295 K	247K	201 K	101 K	51 K	29 K
Drude	$\omega_{p,D}$	5,440	5,900	6,300	6,700	6,750	6,750
(cm^{-1})	Γ_D	550	480	430	320	300	300
	$\omega_{p,1}$	515	500	500	300	300	200
	ω_1	165	165	165	160	159	159
	Γ_1	35	35	35	16	16	12
Phonons	$\omega_{p,2}$	1,150	1,060	1,100	1,170	1,250	1,150
(cm^{-1})	ω_2	337	345	345	345	345	345
	Γ_2	80	70	65	80	80	80
	$\omega_{p,3}$	1,100	1,160	1,200	1,300	1,400	1,300
	ω_3	550	555	555	555	555	555
	Γ_3	110	115	110	120	110	110

As mentioned before, as the temperature is lowered from room temperature to 28 K, certain portion of the spectral weight above 5 000 cm^{-1} is transferred to

the region below 5 000 cm^{-1}, *i.e.* both the Drude and midinfrared part in the two-component model. The distribution of transferred spectral weight to the above two parts as a function of temperature was shown in Figure 4.13. $t^{(x)}(T)$ ($T <$295 K) is defined as following,

$$t^{(x)}(T) = \frac{N_{eff}^{(x)}(T) - N_{eff}^{(x)}(295K)}{N_{eff}^{5000\ cm^{-1}}(T) - N_{eff}^{5000\ cm^{-1}}(295K)}, \qquad (4.3)$$

where x represents the Drude part or the MIR part and $N_{eff}^{(MIR)}(T) = N_{eff}^{5000\ cm^{-1}}(T) - N_{eff}^{(D)}(T)$. $N_{eff}^{(D)}(T)$ is associated with the square of the Drude plasma frequency in Table 4.1 based on the sum rule in Equation 2.13 and 2.14. $N_{eff}^{5000\ cm^{-1}}(T)$ is the partial spectral weight integrated up to 5 000 cm^{-1} and, thus, $N_{eff}^{(MIR)}(T)$ represents the partial spectral weight of the MIR part, between the Drude part and 5 000 cm^{-1}. As shown in Figure 4.13, the transferred spectral weight as temperature decreases goes to the Drude and MIR part in almost equal amounts at high and intermediate temperatures. While as temperature is lowered further, the transferred spectral weight prefers moving to the MIR part rather than the Drude part.

Analogously, the paramagnetic phase of CeTiO$_{3.04}$ and the metallic phase of V$_2$O$_3$ both exhibit conductivity anomalies as the temperature is decreased (Katsufuji and Tokura, 2000, Rozenberg et al., 1995). However, the origin of the anomalous feature is still a controversial issue. Rozenberg et al. (1995) treated the Hubbard model in dynamical mean field theory (DMFT) and predicted an increase of spectral weight as T is decreased in the correlated metallic states which is in good agreement with the experimental results of V$_2$O$_3$. However, the solution of the DMFT also shows that, in the metallic states, a coherent peak appears in the middle of the LH and UH bands. Nevertheless, in our proposed scheme, the coherent component in the optical conductivity corresponds to the partially-filled LH band. In our point of view,
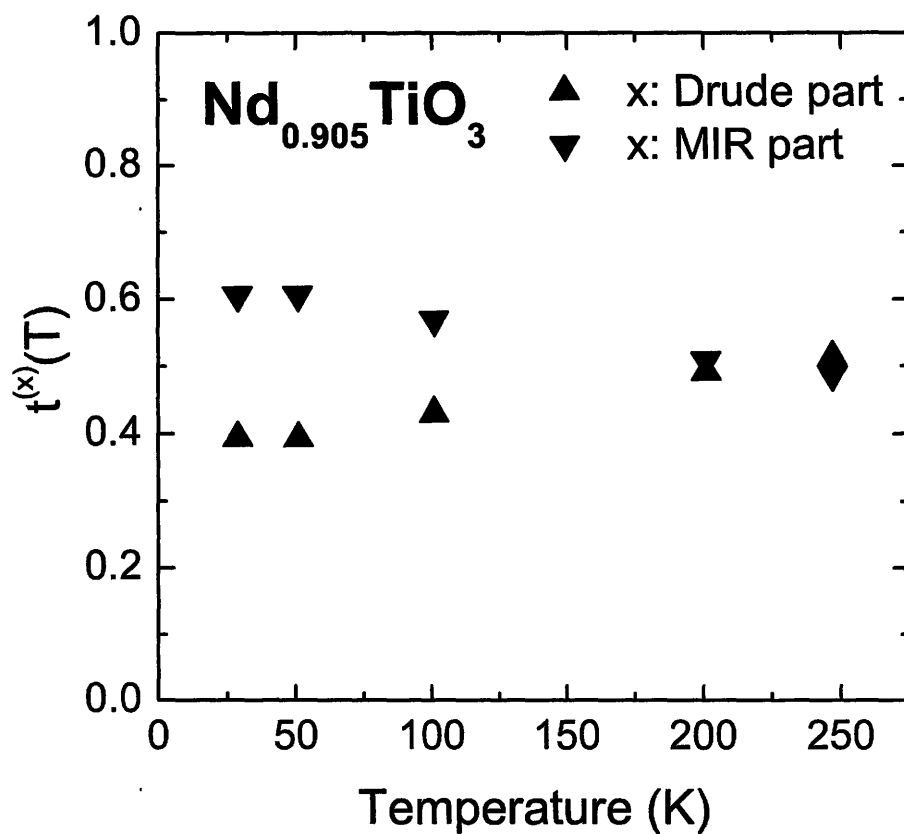
Figure 4.13 The distribution of the transferred spectral weight, from region above 5000 cm^{-1} to that below 5 000 cm^{-1}, in both the Drude and MIR parts as a function of temperature.

decreasing temperature induces an increase of quasi-particle spectral weight at E_F and a progress of spectral weight in the mid-gap state according to the schematic electronic structure in Figure 4.4.

4.3.2   Fermi-Liquid Behavior

In addition to the two-component model discussed in Section 4.3.1, we can also use the extended Drude model to describe the features of the optical conductivity at low frequencies. The calculated frequency-dependent scattering rate of the metallic sample is shown in Figure 4.14. To clearly illustrate the low frequency part of the scattering rate spectrum, all the phonon contributions have been removed from the complex conductivity. Around 800 cm^{-1}, a inflexion-like feature appears at all the temperatures, which may correspond to a different type of inelastic scattering process or an interband transition in the two-component model. In this thesis, we will only focus on the low frequency region of the scattering rate spectrum in the following analysis.

The dc resistivity of $Nd_{0.905}TiO_3$ shows Fermi-liquid-like behavior at intermediate and high temperatures, increasing quadratically with temperature. To verify this relation, we plot the scattering rate spectra as a function of frequency squared in Figure 4.15(a). According to the Fermi-liquid theory (Pines and Nozieres, 1966),

$$\hbar/\tau(\omega, T) = \hbar/\tau_0 + \alpha(k_B T)^2 + \beta(\hbar\omega)^2, \tag{4.4}$$

where, $\alpha/\beta = \pi^2 \simeq 9.87$. In Figure 4.15(a) the curves seem to be parallel to each other. Moreover, the scattering rate shows a approximately linear dependence on ω^2 below 0.1 eV at all the temperatures, though with some deviation at the lowest three temperatures. (The dc resistivity data also shows a non Fermi-liquid behavior
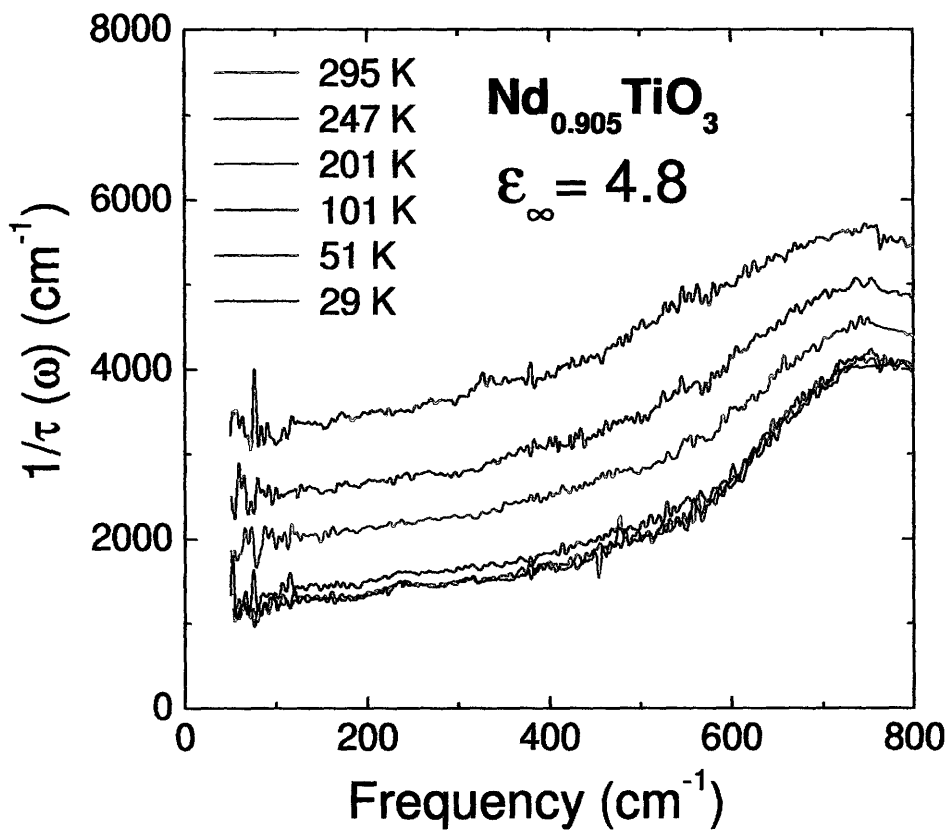
Figure 4.14 The frequency-dependent scattering rate at different temperatures for $Nd_{0.905}TiO_3$, obtained from the extended Drude model. ϵ_∞ was found to be 4.8 from the ϵ_1 spectrum.
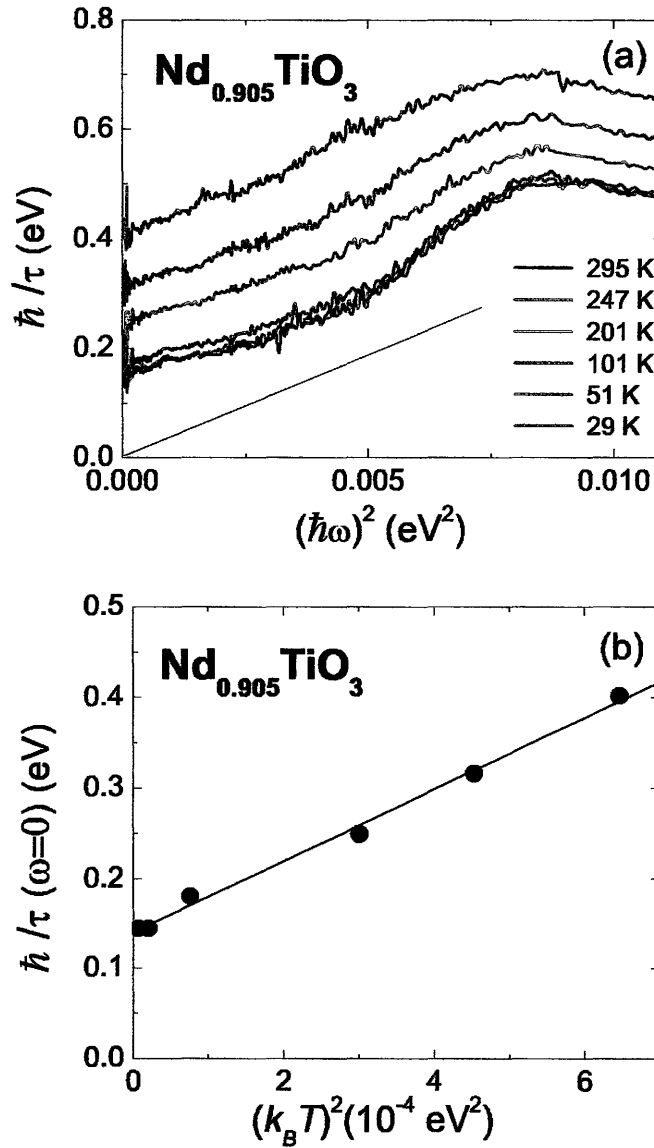
Figure 4.15 (a) Behavior of the scattering rate as a function of frequency squared at different temperatures. The solid line shows a least-squares fit to the room-temperature data. (b) The plot of the scattering rate at zero frequency versus temperature squared for $Nd_{0.905}TiO_3$. The solid line is a least-squares fit to the closed circles.

at low temperatures in Figure 4.9) The above features are consistent with the Fermi-liquid theory according to Equation 4.4. By least-square fits to the room-temperature curve, we estimate the coefficient of $(\hbar\omega)^2$ to be $\beta = 37.38$ eV^{-1}. In Figure 4.15(b), we plot the behavior of the zero-frequency scattering rate with T^2 and the least-squares fit shows the coefficient of $(k_BT)^2$ is $\alpha = 395.2$ eV^{-1}. As a result, α/β is 10.6 for $Nd_{0.905}TiO_3$ in our study, which is only 7 % off the theoretical prediction. Consequently, considering the experimental errors in our study, the correlated metal, $Nd_{0.905}TiO_3$, is consistent with the Fermi-liquid theory in the low frequency limit. This kind of behavior has also been found in the paramagnetic metal $Ce_{0.95}Ca_{0.05}TiO_{3.04}$ (Katsufuji and Tokura, 1999).

Chapter 5

CONCLUSION AND FURTHER STUDIES

In conclusion, we investigated the doping and temperature-dependent optical properties of the hole-doped Mott insulator $Nd_{1-x}TiO_3$ at three doping levels ($x = 0.019, 0.046$ and 0.095) at six different temperatures. There are obvious differences between the titanate system and superconducting cuprates. This is not surprising since the cuprates are hole or electron doped CT insulators and they have 2D layer structures, while $Nd_{1-x}TiO_3$ is a 3D hole doped MH insulator. As mentioned in Section 4.2.2, further studies on highly-doped samples are necessary to make a complete comparison between the two systems. We suggest mid-gap states develop inside the Hubbard gap as hole concentration increases in the current system as clarified in the proposed picture of schematic electronic structures of $Nd_{1-x}TiO_3$. In order to determine whether the small gap between the LHB and the mid-gap state will disappear with doping or not, studies on highly-doped samples are needed. Meanwhile, our study confirms that the rate of spectral weight transfer from MH excitations to the Drude and MIR excitations with doping depends on the electron correlation strength

of the parent insulator. Furthermore, the correlated metallic sample ($x = 0.095$) shows a Fermi-liquid behavior in the low-frequency limit and an anomalous enhancement of spectral weight with decreasing temperature as well, which may be the prediction of the dynamical mean field theory of the Hubbard model. To verify whether the Fermi-liquid behavior is a common property of the titanates or not, we need to investigate the temperature-dependent spectra of correlated metallic samples in other series of titanates.

References

Allen, P. B. (1971). *Phys. Rev. B*, 3, 305.

Arima, T., Tokura, Y., and Torrance, J. B. (1993). *Phys. Rev. B*, 48, 17006.

Bednorz, J. G. and Müller, K. A. (1986). *Z. Phys. B*, 64, 189.

Crandles, D. A., Timusk, T., Garrett, J. D., and Greedan, J. E. (1992). *Phys. C*, 201, 407.

Crandles, D. A., Timusk, T., Garrett, J. D., and Greedan, J. E. (1994). *Phys. Rev. B*, 49, 16207.

Eskes, H., Meinders, M. B. J., and Sawatzky, G. A. (1991). *Phys. Rev. Lett.*, 67, 1035.

Fujimori, A. (1992). *Jpn. J. Appl. Phys.*, 7, 125.

Homes, C. C., Reedyk, M. A., Crandles, D. A., and Timusk, T. (1993). *Appl. Opt.*, 32, 2976.

Hubbard, J. (1963). *Proc. R. Soc. London*, A 276, 238.

Hubbard, J. (1964a). *Proc. R. Soc. London*, A 277, 237.

Hubbard, J. (1964b). *Proc. R. Soc. London*, A 281, 401.

Hwang, J., Yang, J., Timusk, T., and Chou, F. C. (2005a). *Phys. Rev. B*, 72, 024549.

Hwang, J., Yang, J., Timusk, T., Sharapov, S. G., Carbotte, J. P., Bonn, D. A., Liang, R., and Hardy, W. N. (July 27, 2005b). *Submitted to Phys. Rev. B*.

Imada, M., Fujimori, A., and Tokura, Y. (1998). *Rev. Mod. Phys.*, 70, 1039.

Katsufuji, T., Okimito, Y., and Tokura, Y. (1995). *Phys. Rev. Lett.*, 75, 3497.

Katsufuji, T. and Tokura, Y. (1999). *Phys. Rev. B*, 60, 7673.

Katsufuji, T. and Tokura, Y. (2000). *Phys. Rev. B*, 62, 10797.

Kittel, C. (1976). *Introduction to Solid State Physics*. John Wiley and Sons Inc., New York, 5 edition.

Klejnberg, A. and Spalek, J. (2000). *Phys. Rev. B*, 61, 15542.

Kolodiazhnyi, T., Hwang, J., and Timusk, T. (2004). *Private Communication*.

McLean, D. A., Ng, H.-N., and Greedan, J. E. (1979). *J. Solid State Chem.*, 30, 35.

Morikawa, K., Mizokawa, T., Fujimori, A., Taguchi, Y., and Tokura, Y. (1996). *Phys. Rev. B*, 54, 8446.

Mott, N. F. (1949). *Proc. Phys. Soc. London*, A 62, 416.

Mott, N. F. (1956). *Can. J. Phys.*, 34, 1356.

Mott, N. F. (1961). *Philos. Mag.*, 6, 287.

Mott, N. F. (1974). *Metal-Insulator Transitions*. London: Taylor and Francis Ltd.

Okimoto, Y., Katsufuji, T., Okada, Y., Arima, T., and Tokura, Y. (1995). *Phys. Rev. B*, 51, 9581.

Ortolani, M., Calvani, P., and Lupi, S. (2005). *Phys. Rev. Lett.*, 94, 067002.

Pines, D. and Nozieres, P. (1966). *The Theory of Quantum Liquids.* Benjamin, New York.

Robey, S. W., Henrich, V. E., Eylem, C., and Eichhorn, B. W. (1995). *Phys. Rev. B*, 52, 2395.

Rozenberg, M. J., Kotliar, G., Kajueter, H., Thomas, G. A., Rapkine, D. H., Honig, J. M., and Metcalf, P. (1995). *Phys. Rev. Lett.*, 75, 105.

Schiffer, P., Ramirez, A. P., Bao, W., and Cheong, S.-W. (1994). *Phys. Rev. Lett*, 75, 3336.

Sefat, A. S. (2005). Ph.D. Thesis: Magnetic and Electronic Transitions in $Nd_{1-x}TiO_3$: A Study of Correlation Effects. McMaster Univ., Hamilton, ON.

Timusk, T. and Tanner, D. B. (1989). *Physical Properties of High Temperature Superconductors I.* World Scientific Publishing Co. Pte. Ltd.

Uchida, S., Ido, T., Takagi, H., Arima, T., Tokura, Y., and Tajima, S. (1991). *Phys. Rev. B*, 43, 7942.

Yokoya, T., Sato, T., Fujisawa, H., Takahashi, T., Chainani, A., and Onoda, M. (1999). *Phys. Rev. B*, 59, 1815.

Zaanen, J., Sawatzky, G. A., and Allen, J. W. (1985). *Phys. Rev. Lett.*, 55, 418.

Appendix A

Matlab programs

```
***********************************************************************
Filename: RPH2E.m

***********************************************************************
% Calculate $\epsilon_1$ and $\epsilon_2$ from reflectance and phase factor
% and save the result into the output file;
function RPH2E(fname)
[f,R,p,header]=getspec(fname);
N=(1+R.^0.5.*exp(i*p))./(1-R.^0.5.*exp(i*p));
eps1=real(N.^2);
eps2=imag(N.^2);
filename=input('Enter the output filename > ','s');
[m,n]=size(header);
fid=fopen(filename,'w');
for l=1:m-1
    for j=1:n
        fprintf(fid,'%c',header(l,j));
```

```
        end
end
fprintf(fid,'\n');
fprintf(fid,'Freq         epsilon_1        epsilon_2 \n');
fprintf(fid,'/* \n');
fprintf(fid,'%8.4f        %8.4f        %8.4f \n',[f,eps1,eps2]');
fclose(fid);
% plot epsilon figures;
hold on
plot(f,eps1)
plot(f,eps2,'g')
xlabel('Frequency (cm∧{-1})')
ylabel('epsilon1')
axis([50 40000 -7000 10])
legend('eps1','eps2')
hold off
***********************************************************************
Filename: E2S.m
***********************************************************************
% Calculate σ_1, σ_2 from epsilon data
% and save the result into the output file;
function E2S(fname)
[f,eps1,eps2,header]=getspec(fname);
eps_inf=input('Enter the value of epsilon infinity > ');
sig1=f.*eps2/60;
sig2=f.*(eps_inf-eps1)/60;
```

```
filename=input('Enter the output filename > ','s');

[m,n]=size(header);

fid=fopen(filename,'w');

for l=1:m-1

    for j=1:n

        fprintf(fid,'%c',header(l,j));

    end

end

fprintf(fid,'\n');

fprintf(fid,'epsilon_infinity=%f \n',eps_inf);

fprintf(fid,'Freq        sigma_1        sigma_2 \n');

fprintf(fid,'/* \n');

fprintf(fid,'%8.4f        %8.4f        %8.4f \n',[f,sig1,sig2]');

fclose(fid);

% plot sigma_ figures;

hold on

plot(f,sig1)

xlabel('Frequency (cm^{-1})')

ylabel('\sigma_{1}(\omega)(\Omega^{-1}cm^{-1})')

axis([55 35000 0 5000])

legend('sigma1')

hold off

*****************************************************************

Filename: S2T.m

*****************************************************************

% Calculate 1/\tau, effective mass from sigma data
```

```
% and save the result into the output file;
function S2T(fname)
[f,sig1,sig2,header]=getspec(fname);
plasma_freq=input('Enter the value of plasma frequency(cm∧{-1}) > ');
S=sig1+i*sig2;
tao_inv=plasma_freq∧{2}*real(1./S)/60;
eff_mass=-plasma_freq∧{2}*imag(1./S)./f/60;
filename=input('Enter the output filename > ','s');
[m,n]=size(header);
fid=fopen(filename,'w');
for l=1:m-1
    for j=1:n
        fprintf(fid,'%c',header(l,j));
    end
end
fprintf(fid,'\n');
fprintf(fid,'plasma frequency=%f cm∧{-1} \n',plasma_freq);
fprintf(fid,'Freq        scattering_rate        effective_mass \n');
fprintf(fid,'/* \n');
fprintf(fid,'%8.4        %8.4f        %8.4f \n',[f,tao_inv,eff_mass]');
fclose(fid);
% plot scattering_rate figures;
hold on
plot(f,tao_inv)
xlabel('Frequency (cm∧{-1})')
ylabel('1/\tau(\omega)(cm∧{-1})')
```

```
axis([0 5000 0 6000])

hold off

**********************************************************************

Filename: S2Neff.m

**********************************************************************

% Calculate spectral weight (number of effective electrons per atom)

% from the sigma data and save the result into the output file;

function S2Neff(fname)

[f,sig1,sig2,header]=getspec(fname);

V_atom=input('Enter the volume (A^{3}) per atom > ');

Neff=4.26E-10*V_atom*cumtrapz(f,sig1);

filename=input('Enter the output filename > ','s');

[m,n]=size(header);

fid=fopen(filename,'w');

for l=1:m-1

    for j=1:n

        fprintf(fid,'%c',header(l,j));

    end

end

fprintf(fid,'\n');

fprintf(fid,'The volume per atom =%f A^{3} \n',V_atom);

fprintf(fid,'Freq        Neff \n');

fprintf(fid,'/* \n');

fprintf(fid,'%8.4f        %8.4f \n',[f,Neff]');

fclose(fid);

% plot N_eff figures;
```

```
hold on

plot(f,Neff)

xlabel('Frequency (cm^{-1})')

ylabel('N_{eff}')

axis([0 30000 0 1]);

hold off
```

****

Filename: Wp.m

****

```
% Calculate Plasma Frequency Wp from the σ₁ data

% and save the result into the output file;

function Wp(fname)

[f,sig1,sig2,header]=getspec(fname);

Wc=input('Enter the value of Wc > ');

% find the dimension of f < Wc;

dim=0;

while f(dim+1)<=Wc

      dim=dim+1;

end

% calculate plasma frequency Wp;

int=cumtrapz(f,sig1);

Wp=sqrt(120/pi*int(dim));

filename=input('Enter the output filename > ','s');

[m,n]=size(header);

fid=fopen(filename,'w');

for l=1:m-1
```

```
    for j=1:n
        fprintf(fid,'%c',header(1,j));
    end
end
fprintf(fid,'\n');
fprintf(fid,'The cutoff frequency Wc=%f cm∧{-1} \n',Wc);
fprintf(fid,'Wp=\n');
fprintf(fid,'%8.4f\n',Wp');
fclose(fid)
********************************************************************
Filename: getspec.m
********************************************************************
% Get all the three columns after /* from the fname file
% stored in the first three parameters;
% get the lines before /* and store them in header
% which has nc strings;
function [f,R,p,header]=getspec(fname)
fid=fopen(fname);
nc=1;
% find tanner flag /* and store lines before /* into header;
flag=0;
while ~ feof(fid);
    line=fgetl(fid);
    if (line(1)=='/')&(line(2)=='*')
        flag=nc;
        break
```

```
    else
      for j=1:length(line)
          header(nc,j)=line(j);
      end
      nc=nc+1;
    end
end
frewind(fid);
if(flag==0)
    fprintf(1,'%s \n','tanner flag not found')
else
% read data after /* and save them to
% f,R and p(the first three parameters)
[f,R,p]=textread(fname,'%f    %f    %f','headerlines',flag);
fclose(fid);
end
```

Appendix B

Hagen-Rubens Relations

In chapter 2, we got the Drude conductivity in Equation 2.20 as:

$$\sigma_1(\omega) = \frac{\omega_p^2 \Gamma}{4\pi(\omega^2 + \Gamma^2)}. \qquad (B.1)$$

If $\omega \ll \Gamma$, σ_1 becomes

$$\sigma_1(\omega) \simeq \frac{\omega_p^2}{4\pi\Gamma}, \qquad (B.2)$$

which is a constant. Since $\epsilon_1 \ll \epsilon_2$, Equation 2.4 becomes

$$n + i\kappa \simeq \sqrt{i\epsilon_2} = \sqrt{\frac{i4\pi\sigma_1}{\omega}}. \qquad (B.3)$$

As a result,

$$n \simeq \kappa \simeq \sqrt{\frac{2\pi\sigma_1}{\omega}} \qquad (B.4)$$

From Equation 2.10, one gets the Hagen-Rubens relation:

$$R(\omega) \simeq 1 - \frac{2}{n} \simeq 1 - \sqrt{\frac{2\omega}{\pi\sigma_1}}. \qquad (B.5)$$